3

Growth and Transport Properties of Tetradymite Thin Films

Hang Chi, Wei Liu, and Ctirad Uher
University of Michigan

CONTENTS

3.1 Introduction

Interest in thermoelectric (TE) properties of tetradymite-type materials, that is, Bi_2Se_3, Bi_2Te_3, and Sb_2Te_3, originated from the work of Goldsmid and coworkers on bulk forms of the structure in the mid-1950s [1]. The excellent dimensionless thermoelectric figure of merit ZT for both n-type and p-type tetradymite solid solutions has enabled this material family to be one of the most successfully commercialized TE systems, especially for low-temperature applications [2,3]. Motivated by the increasing demand for alternative green energy, much research and development have been done in the past two decades toward advancing efficient synthesis processes [4], device fabrication [5], and physical property characterization [6]. These efforts have, in turn, significantly deepened the understanding and improved the performance of TE materials. Indeed, the state-of-the-art p-type ZT has reached ~1.8 at 320 K in the bulk nanocomposite form of this classic TE material system [7–9].

As proposed by Dresselhaus and colleagues in the early 1990s [10–12], materials with lower-dimensional characteristics, such as 2D superlattices (SLs), 1D nanowires, and 0D quantum dots, may possess significantly enhanced TE properties and have been intensively studied to achieve (1) reduction in thermal conductivity (e.g., by all-scale hierarchical phonon scattering [13]) and (2) enhancement in power factor (via formation of band resonant states [14], quantum confinement [15], modulation doping [16], energy filtering [17], and other novel mechanisms [18]). A spectacular $ZT \sim 2.4$ at 300 K was claimed in 2001 for p-type Bi_2Te_3/Sb_2Te_3 SLs [19]. Despite the fact that such impressive ZT values on SLs have never been reproduced by intense efforts worldwide [20], the possibility of enhancing TE performance by decoupling electronic and thermal transport processes with reduced dimensionality has boosted the fabrication of tetradymite-type TE films and SLs.

Recently, topologically nontrivial materials have attracted heightened attention around the globe, owing to their potential of revealing new physical phenomena and prospects for developing next-generation electronics. Ever since their discovery [21–24], tetradymite-based 3D topological insulators (TIs) have stimulated worldwide interest in surface states (SSs) arising from the strong spin-orbital coupling and time-reversal symmetry [25–27]. Immune to perturbations of weak electromagnetic fields and/or nonmagnetic impurities, the relaxation times dominating surface transport can be much enhanced, resulting in a nondissipative surface conduction. The (1) Dirac-like linear energy dispersion and (2) spin-momentum locking are the two key features of these topologically protected SSs, which have been confirmed by angle-resolved photoemission spectroscopy (ARPES) and scanning tunneling microscopy (STM) experiments. Transport-wise, weak antilocalization (WAL) effect and Shubnikov-de Haas oscillations in the TE tensors (resistivity and thermopower under applied magnetic fields) have been effectively used to characterize the SSs of tetradymite-type TIs [28–33].

Despite the success in observing all these transport hallmarks in laboratories, practical applications utilizing SSs still seem rather remote and hindered by the presence of predominant bulk carriers (~10^{19} cm^{-3}, due to intrinsic antisite defects and/or vacancies in near-equilibrium grown tetradymite-type structures). However, remarkable progress is being made in thin films prepared under far-from-equilibrium conditions, whose large surface/volume ratio naturally favors the manifestation of surface conduction. More importantly, it is possible to identify deposition protocols that depress the undesired background carrier density by fine tuning constituent stoichiometry, film thickness, and annealing temperature, that is, the material control parameters that are not easily accessible during the growth of bulk crystals.

In the following sections of this chapter, we will describe in more details the tetradymite-type material structure, which present recent developments regarding the deposition of tetradymite-type thin films and SLs, and summarize their transport properties. Such studies may shed more light on prospects of further enhancing the performance of tetradymite-type thin-film TEs.

3.2 Tetradymite Structure

Combining pnictogen (A^V = Bi, Sb) and chalcogen (B^{VI} = Te, Se, S) atoms in the 2:3 ratio results in the formation of a trigonal $A_2^V B_3^{VI}$ crystal with the space group $R\bar{3}m$ (D_{3d}^5, No. 166). As shown in Figure 3.1a, $A_2^V B_3^{VI}$ has a layered structure with a [B^{VI}(1)–A^V–B^{VI}(2)–A^V–B^{VI}(1)] type of quintuple layers (QLs, ~1 nm thick, within which the bonding is of ionic-covalent nature) connected by a weak van der Waals (vdW) interaction between neighboring quintuple layers, often referred to as the tetradymite lattice. The unit cell is the conventional hexagonal cell, which can be adopted for all the 25 trigonal space groups (No. 143–167 [34]). The cations occupy the Wyckoff 6c sites A^V (0, 0, z_A ~ 0.4), while the anions are located at 6c sites B^{VI}(1) (0, 0, z_B ~ 0.2) and 3a sites B^{VI}(2) (0, 0, 0). There are, however, seven space groups in the trigonal crystal system (No. 146, 148, 155, 160, 161, 166, and 167) that possess a rhombohedral lattice, whose unit cells can be reduced from the hexagonal cell (Figure 3.1b, a volume 3 supercell containing three lattice points) to a primitive rhombohedral cell (Figure 3.1c). The lattice parameters (a, b, c, α, β, γ), coordinates (x, y, z), directions [uvw], and planes (hkl) in the hexagonal ($a_H = b_H \neq c_H$, $\alpha_H = \beta_H = 90°$, $\gamma_H = 120°$, using the three-index symbols) and the rhombohedral ($a_R = b_R = c_R$, $\alpha_R = \beta_R = \gamma_R$) representations can be converted back and forth via the following relations:
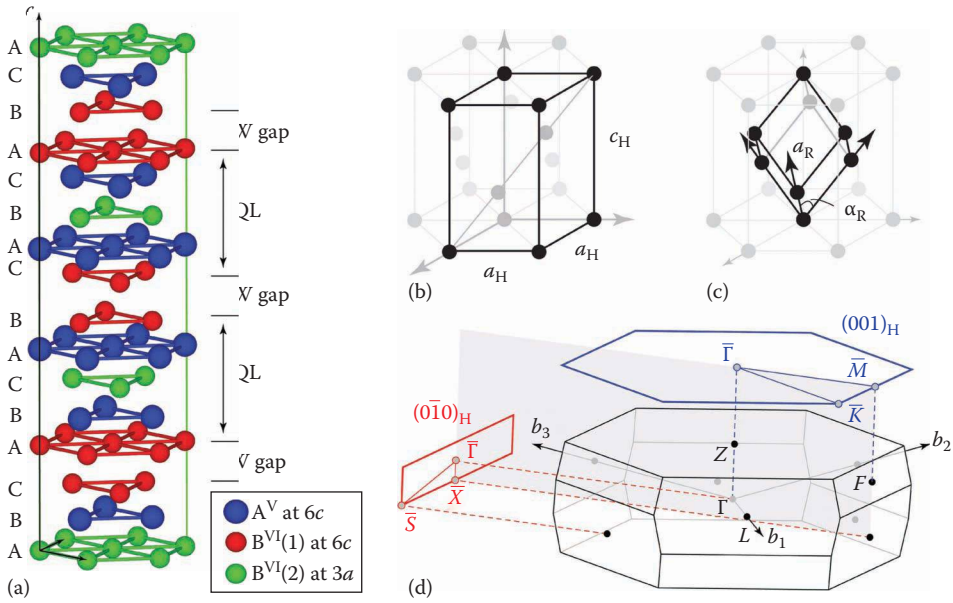
FIGURE 3.1
(a) Tetradymite-type crystal structure with [$\cdots$B^{VI}(1)–A^{V}–B^{VI}(2)–A^{V}–B^{VI}(1)$\cdots$] quintuple layers that are separated by van der Waals gaps, along with its (b) conventional hexagonal cell, (c) primitive rhombohedral cell, and (d) the first Brillouin zone for 3D bulk and selected 2D surfaces.

hexagonal → rhombohedral

$$a_R = \frac{1}{3}\sqrt{3a_H^2 + c_H^2}, \quad \alpha_R = 2\sin^{-1}\left(\frac{3}{2\sqrt{3+\left(c_H^2/a_H^2\right)}}\right),$$

$$x_R, y_R, z_R = x_H + z_H, -x_H + y_H + z_H, -y_H + z_H,$$

$$[u_R \quad v_R \quad w_R] = [u_H + w_H \quad -u_H + v_H + w_H \quad -v_H + w_H],$$

$$(h_R \quad k_R \quad l_R) = \frac{1}{3}(2h_H + k_H + l_H \quad -h_H + k_H + l_H \quad -h_H - 2k_H + l_H) \tag{3.1}$$

and
rhombohedral → hexagonal

$$a_H = 2a_R \sin\left(\frac{\alpha_R}{2}\right), \quad c_H = a_R\sqrt{3 + 6\cos\alpha_R},$$

$$x_H, y_H, z_H = (0,0,0; \tfrac{2}{3}, \tfrac{1}{3}, \tfrac{1}{3}; \tfrac{1}{3}, \tfrac{2}{3}, \tfrac{2}{3})$$

$$+ (2x_R - y_R - z_R)/3, (x_R + y_R - 2z_R)/3, (x_R + y_R + z_R)/3,$$

$$[u_H \quad v_H \quad w_H] = \frac{1}{3}[2u_R - v_R - w_R \quad u_R + v_R - 2w_R \quad u_R + v_R + w_R],$$

$$(h_H \quad k_H \quad l_H) = (h_R - k_R \quad k_R - l_R \quad h_R + k_R + l_R) \tag{3.2}$$

Specifically, in the Cartesian coordinate system constructed by the binary (x), bisectrix (y), and trigonal (z) axes, the rhombohedral primitive unit vectors $\boldsymbol{a}_i$ (in terms of $\hat{x}$, $\hat{y}$, $\hat{z}$) and the reciprocal lattice vectors $\boldsymbol{b}_j$ (in the space of $\hat{k}_x$, $\hat{k}_y$, $\hat{k}_z$, where $\boldsymbol{a}_i \cdot \boldsymbol{b}_j = 2\pi\, \delta_{ij}$) are given in the following equation:

$$\boldsymbol{a}_1 = \left(\frac{a}{2}, \frac{a}{2\sqrt{3}}, \frac{c}{3}\right), \quad \boldsymbol{a}_2 = \left(-\frac{a}{2}, \frac{a}{2\sqrt{3}}, \frac{c}{3}\right), \quad \boldsymbol{a}_3 = \left(0, -\frac{a}{\sqrt{3}}, \frac{c}{3}\right);$$

$$\boldsymbol{b}_1 = \frac{2\pi}{a}\left(1, \frac{1}{\sqrt{3}}, \frac{a}{c}\right), \quad \boldsymbol{b}_2 = \frac{2\pi}{a}\left(-1, \frac{1}{\sqrt{3}}, \frac{a}{c}\right), \quad \boldsymbol{b}_3 = \frac{2\pi}{a}\left(0, -\frac{2}{\sqrt{3}}, \frac{a}{c}\right). \tag{3.3}$$

When expressed in fractions of $\boldsymbol{b}_j$, Γ (0, 0, 0), L (½, 0, 0), F (½, ½, 0), and Z (½, ½, ½) are the four time-reversal invariant momentum high-symmetry points in the 3D first Brillouin zone (BZ) for the bulk tetradymite-type structure. As illustrated in Figure 3.1d, two important low-index 2D BZ, on the hexagonal $(111)_R$ $[(001)_H]$ and the rectangular $(\bar{1}\bar{1}2)_R$ $[(0\bar{1}0)_H]$ surfaces, are constructed via projection from the 3D BZ.

The best known tetradymite-type structures are Bi_2Se_3 [35], Bi_2Te_3 [36], and Sb_2Te_3 [37], along with ternary Bi_2Te_2Se [38], Bi_2Se_2Te [39], and $Bi_2Te_{1.6}S_{1.4}$ (where Te and S species mix on the anion $6c$ sites) [40] and their solid solutions—for example, $(Bi_{0.58}Sb_{1.42})(Se_{0.12}Te_{2.88})$ [41]. Other binary combinations, that is, Bi_2S_3 [42], Sb_2Se_3 [43], and Sb_2S_3 [44], result in orthorhombic structures with the space group *Pnma* (D_{2h}^{16}, No. 62). Note that elemental Bi [45] and Sb [46] crystals also have the rhombohedral $R\bar{3}m$ (D_{3d}^5, No. 166) lattice, which may be used as a buffer layer during the growth of tetradymite-type thin films. Pure Te [47] and Se [48] crystallize in a trigonal $P3_121$ (D_3^4, No. 152) structure (often a convenient choice for capping layers in order to protect as-grown thin films for *ex situ* characterizations), while crystalline S usually takes the S_8 form [49] with orthorhombic *Fddd* (D_{2h}^{24}, No. 70) symmetry. A summary of the crystallographic information for these tetradymite-related structures is tabulated in Table 3.1.

All three binary tetradymite-type compounds are semiconductors with small band gaps of ~0.30 eV (Bi_2Se_3), 0.13 eV (Bi_2Te_3), and 0.28 eV (Sb_2Te_3), respectively. Bulk crystals grown from stoichiometric melts under near-equilibrium conditions (via Bridgman, Czochralski, and/or floating zone type of methods) all possess rather high background charge carrier densities. Due to the presence of selenium vacancies ($V_{Se}^{\cdot\cdot}$, a double-electron donor), the electrical conduction of pristine Bi_2Se_3 is dominated by electrons (*n*-type), with a room temperature electron density ~10^{19} cm^{-3}. Owing to the native anti-site defects (Bi'_{Te} or Sb'_{Te}, a single-hole acceptor), pure Bi_2Te_3 and Sb_2Te_3 bulk crystals are usually *p*-type with room temperature hole densities of ~10^{19} and ~10^{20} cm^{-3}, respectively. While Bi_2Se_3 (Bi_2Te_3) may be tuned into a *p*-type (*n*-type) conductor through doping and/or intentional off-stoichiometric growth, there are no reports on preparing an *n*-type Sb_2Te_3. Furthermore, molecular beam epitaxy (MBE)–grown Bi_2Te_3 thin films (as shown in the following) are dominantly *n*-type, while Bi_2Se_3 and Sb_2Te_3 films are still *n*-type and *p*-type, respectively. This is argued as a result of the fact that the optimized growth temperature for Bi_2Te_3 is usually much lower than the melting temperature, which favors interstitial Bi atoms or Te vacancies more than the formation of antisite defects, driving the system *n*-type.

Tetradymite-type compounds have a strong anisotropy in their transport properties inherited from the anisotropy in the crystal structures, see Figure 3.1a. The in-plane

TABLE 3.1

Crystallographic Information[a] for Tetradymite-Related Materials

Materials	SG	ICSD	Reference	a_H (Å)	c_H (Å)	Element	x_H	y_H	z_H
Bi_2Se_3	166	165226	[35]	4.1355	28.6150	Bi	0.0000	0.0000	0.4006
						Se_1	0.0000	0.0000	0.2109
						Se_2	0.0000	0.0000	0.0000
Bi_2Te_3	166	184631	[36]	4.3896	30.5019	Bi	0.0000	0.0000	0.4004
						Te_1	0.0000	0.0000	0.2094
						Te_2	0.0000	0.0000	0.0000
Sb_2Te_3	166	192780	[37]	4.2706	30.4758	Sb	0.0000	0.0000	0.3986
						Te_1	0.0000	0.0000	0.2122
						Te_2	0.0000	0.0000	0.0000
Bi_2Te_2Se	166	43512	[38]	4.2800	29.8600	Bi	0.0000	0.0000	0.3960
						Te	0.0000	0.0000	0.2120
						Se	0.0000	0.0000	0.0000
Bi_2Se_2Te	166	54838	[39]	4.1830	29.1370	Bi	0.0000	0.0000	0.3981
						Se	0.0000	0.0000	0.2116
						Te	0.0000	0.0000	0.0000
Bi	166	64703	[45]	4.5460	11.8620	Bi	0.0000	0.0000	0.2339
Sb	166	64695	[46]	4.3084	11.2740	Sb	0.0000	0.0000	0.2335
Te	152	65692	[47]	4.4560	5.9210	Te	0.2636	0.0000	0.3333
Se	152	40018	[48]	4.3680	4.9580	Se	0.2254	0.0000	0.3333

[a] Space group, inorganic crystal structure database collection code, hexagonal lattice constants and atomic occupation.

electronic properties are superior while the in-plane lattice thermal conductivity is also much higher than that across the plane. For instance, in the Bi_2Te_3–Sb_2Te_3 system, the anisotropic ratio of electrical conductivity and lattice thermal conductivity is in the range of 2.8–6.3 and 2.0–7.1, respectively [2,50]. Typical in-plane transport properties of bulk tetradymite-type single crystals [51–53] have been summarized in Table 3.2. As we will see, when grown in thin-film form, the film orientation and microstructures also remarkably affect the transport properties.

When it comes to TE applications, it is the solid solutions of these end compounds that are of practical interest. The formation of solid solutions introduces short-range disorder into the structure, which strongly scatters heat-conducting phonons and significantly reduces the lattice thermal conductivity. As a result, the best performing *p*-type tetradymite TE is based on a composition near $Bi_{0.5}Sb_{1.5}Te_3$, while the *n*-type counterpart is close to $Bi_2Te_{2.85}Se_{0.15}$. Progress has been made to further reduce the thermal conductivity by fabricating nanostructured composites. Nanostructures introduced by ball milling and melt spinning have demonstrated a *ZT* ~1.4 (at 373 K) [7] and ~1.5 (at 390 K) [8] in *p*-type BiSbTe nanocomposites. A recent modification of the melt spinning technique (followed by spark plasma sintering) has exploited excessive Te to introduce additional phonon scattering at the grain boundary, which further reduces the thermal conductivity and results in a *ZT* ~1.8 (at 320 K) in *p*-type $Bi_{0.5}Sb_{1.5}Te_3$ [9]. It is of prime interest to adopt and/or redesign these successful recipes for *p*-type structures and apply them to *n*-type forms of tetradymite-type materials to improve their performance.

TABLE 3.2

Transport Properties of Bulk Bi_2Se_3 [51], Bi_2Te_3 [52], and Sb_2Te_3 [53] in the Basal Plane at 300 K

Properties	Bi_2Se_3	Bi_2Te_3	Sb_2Te_3
E_g	~0.30	0.13	0.28
Type	$n(n)$	$p(n)$	$p(p)$
n_H	2.13	1.12	8.92
μ_H	809	351	330
σ	2.76	0.63	4.72
α	−59	245	79
PF	9.61	37.82	29.46
κ	3.10	2.01	4.95
ZT	0.09	0.56	0.18

The electronic band gap, E_g (eV); carrier type for bulk (film); carrier density, n_H (10^{19} cm^{-3}); Hall mobility, μ_H (cm^2 V^{-1} s^{-1}); electrical conductivity, σ (10^5 S m^{-1}); Seebeck coefficient, α (μV K^{-1}); power factor, $PF \equiv \alpha^2\sigma$ (10^{-4} W m^{-1} K^{-2}); thermal conductivity, κ (W m^{-1} K^{-1}); figure of merit, $ZT \equiv \alpha^2\sigma T/\kappa$.

3.3 Thin-Film Growth

Various methods have been reported to prepare tetradymite-type thin films and SLs with tunable TE properties, such as coevaporation (CE) [54–58], electrochemical deposition [59–62], flash evaporation (FE) [63–66], metal organic chemical vapor deposition (MOCVD) [19,67–77], MBE [78–84], nanoalloying (NA) [85–88], pulsed laser deposition (PLD) [89–95], and sputtering [50,96–106]. Generally, CE, FE, MBE, NA, PLD, and sputtering can be classified as physical vapor deposition (PVD) processes. Although they differ in particulars (e.g., how the atomic/molecular plume/fluxes are generated and delivered onto the substrate), these PVD techniques have much in common; the desired compounds form on a heated substrate by supplying flux of molecules or atoms with an appropriate ratio. Therefore, strategies applicable to tetradymite-type film growth in MBE are also suitable for other PVD techniques, while the appropriate deposition parameters may vary case by case. In MOCVD processes, however, besides the substrate temperature and flux rate, other factors such as the selection of precursors, substrate position, and working pressure are also crucial for the growth and quality control of tetradymite-type films. As for electrochemical deposition, postgrowth annealing at elevated temperatures is often mandatory to improve crystallinity and the orientation of films [60].

The crystallographic building block of the $A_2^{V}B_3^{VI}$ thin film is the ~1 nm thick B^{VI}-terminated QL (Figure 3.1a). This also implies that *c*-oriented growth of tetradymite-type film is energetically favored due to the weak vdW interaction between adjacent layers. Benefiting from this feature, the fabricated tetradymite-type films are mostly *c*-oriented regardless of the choice of substrates or deposition techniques. A selection of commonly used single crystal substrates are listed in Table 3.3. In fact, the vdW epitaxial nature of tetradymite-type films is so tolerant that tetradymite-type structures can even be grown on amorphous glass substrates with good quality. Such an intermediate

TABLE 3.3

In-Plane Lattice Mismatch between Tetradymite-Type Films (a_{film}) and a Selection of Substrates ($a_{substrate}$), Defined as $\delta = (a_{film}/a_{substrate} - 1) \times 100\%$

Substrate	$a_{substrate}$ (Å)	$\delta_{Bi_2Se_3}$ (%)	$\delta_{Bi_2Te_3}$ (%)	$\delta_{Sb_2Te_3}$ (%)
Al_2O_3 (0001)	4.7602	−13.1	−7.8	−10.3
BaF_2 (111)	4.3815	−5.6	−0.2	−2.5
Bi (0001)	4.5460	−9.0	−3.4	−6.1
CdTe (111)	4.5840	−9.8	−4.2	−6.8
GaAs (111)	3.9966	+3.5	+9.8	+6.9
Si (111)	3.8400	+7.7	+14.3	+11.2
$SrTiO_3$ (111)	5.5202	−25.1	−20.5	−22.6

tetradymite-type thin film has been recently engineered as a buffer layer for producing II–VI films with unprecedented crystallinity [107]. As demonstrated by da Silva et al., *c*-oriented polycrystalline Bi_2Te_3 films were successfully grown on glass substrates using the CE method [55]. The coevaporated Bi_2Te_3 at 130°C was polycrystalline (Figure 3.2b) with an x-ray diffraction pattern similar to that of powder Bi_2Te_3 (Figure 3.2a), while the film grown at 260°C started to show strong *c*-orientation (Figure 3.2c). Evident from the cross-sectional scanning electron microscopy images, the grain boundary of Bi_2Te_3 films grown at 130°C was rather unclear (even with observable pin holes, Figure 3.2d). Increasing the substrate temperature to 260°C significantly promoted the crystal growth and resulted in a large grain size up to ~500 nm (Figure 3.2e). As shown in Figure 3.2f, reduced Te flux led to degraded growth of the Bi_2Te_3 film, advocating for a Te-rich growth condition in order to effectively compensate the reevaporation of Te from the substrate surface at high temperatures. To achieve high crystallinity and thus improve electronic properties in tetradymite-type films, relatively high-substrate temperature and Te flux were preferred, in agreement with observations using other growth techniques [58,76,82,83].

Regardless of the differences of deposition techniques, recent studies on tetradymite-type thin-film TEs have focused on (1) good crystallinity, (2) controllable carrier density, (3) favorable microstructures, (4) stable and functional SLs, and (5) new phenomena for enhanced TE performances. Among these techniques, MOCVD was first selected to grow tetradymite-type SLs with reported extremely high-*ZT* values in 2001 [19]. However, it was only quite recently that the researchers managed to utilize MBE techniques to reproduce excellent Bi_2Te_3/Sb_2Te_3 SLs with demonstrated good crystallinity [81,108]. Indeed, boosted by the TI research, the MBE technique has produced tetradymite-type films with the best crystallinity, close to that of the best bulk single crystals ever reported. These high-quality films possess strictly *c*-axis orientation, ultrahigh purity in composition, and a noticeably suppressed density of point defects and twin domains [109–114]. The improved film quality is believed to originate from the layer-by-layer growth of films in MBE, which relies on the precise control of growth parameters, such as the ultrahigh vacuum (UHV), flat substrates with extremely clean surfaces, and optimal growth temperature, along with very stable and uniform flux of raw elements.

Due to its unique ability to control an epitaxial growth mode, producing high-quality films using MBE has gained popularity over recent years, despite its expensive nature in terms of construction, operation, and maintenance. As schematically shown in Figure 3.3,

MBE is a thin-film deposition process that takes place in an UHV chamber maintained by a staged continuous pumping system, using a combination of ionic pump, turbomolecular pump, and scroll pump. The chief reason of intentionally choosing only *dry* pumps is to eliminate contaminations from any oil vapors. A cryoshield is often implemented to further improve the vacuum, via the added power of adsorbing atom/molecules on surfaces cooled by flowing liquid nitrogen. Pressure in the growth chamber is read using hot-filament ionization gauges and thermocouple gauges. Potential leaks are monitored by a residue gas analyzer. Resistive baking heaters are installed for regular chamber cleaning. A load/lock entry chamber, separated by a gate valve from the deposition chamber, is designed for fast sample entry and retrieval using a holder/fork mechanism. Chambers with additional functionalities can also be integrated. These include preparation/treatment chambers and characterization chambers. In the most state-of-the-art MBE systems, many advanced characterization probes (e.g., ARPES and STM) are nowadays integrated together with the main MBE chamber, enabling direct *in situ* characterization of films. These recent advances in instrumentation have significantly promoted the study of tetradymite-type thin films.
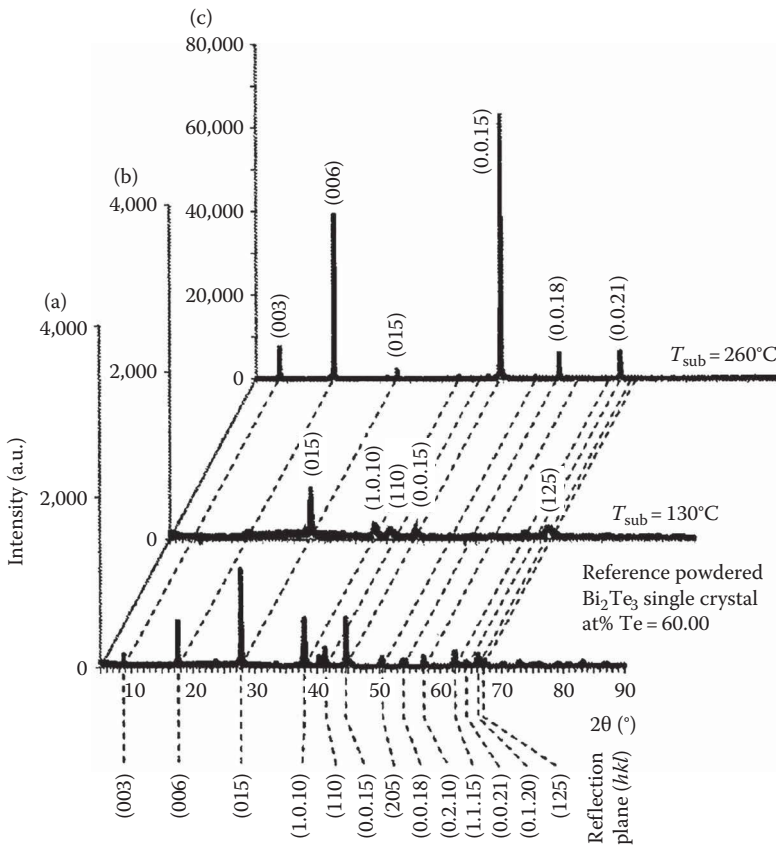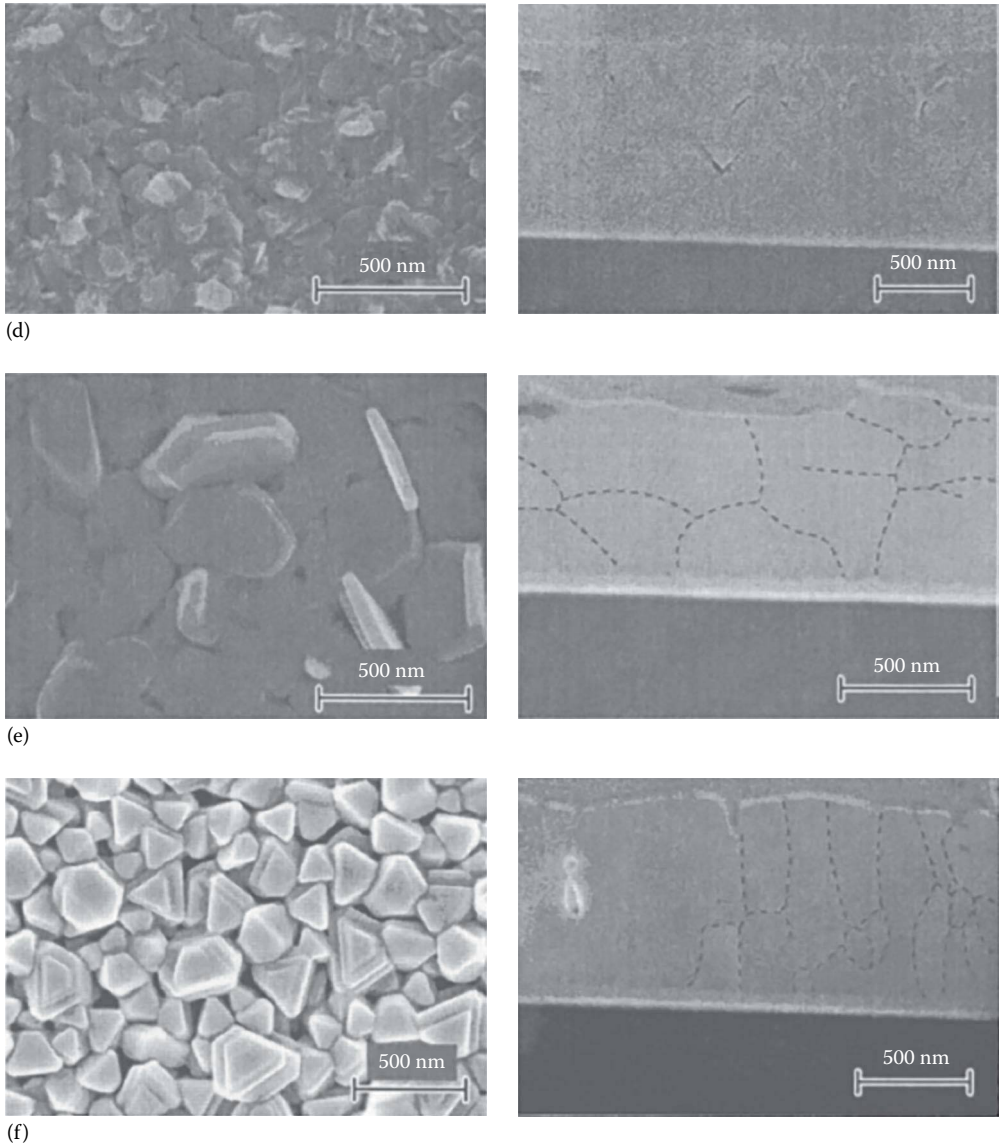

FIGURE 3.2
X-ray diffraction patterns of (a) reference-powdered Bi_2Te_3 and coevaporated Bi_2Te_3 film deposited on a glass substrate at (b) 130°C (at% Te = 60%) and (c) 260°C (at% Te = 60%).   (*Continued*)

FIGURE 3.2 (*Continued*)
Scanning electron microscopy images showing the top and cross section of the coevaporated Bi_2Te_3 films deposited at (d) 130°C (at% Te = 60%), (e) 260°C (at% Te = 60%), and (f) 260°C (at% Te = 54%), respectively. In (e) and (f), the dashed lines at the cross section views highlight grain boundaries. (Reprinted with permission from da Silva, L.W., Kaviany, M., and Uher, C., Thermoelectric performance of films in the bismuth-tellurium and antimony-tellurium systems, *J. Appl. Phys.*, 97, 114903. Copyright 2005, American Institute of Physics.)

Knudsen effusion cells are used to produce carefully controlled atomic/molecular fluxes. These cells, with crucibles loaded with high-purity source materials, are usually integrated through ports at the bottom side of the chamber. Additional miniature electron beam guns can be incorporated for doping by high-melting-point elements. Gas/plasma-type sources may also be installed if desired. In the case of Bi_2Se_3 (Bi_2Te_3), a Bi-containing
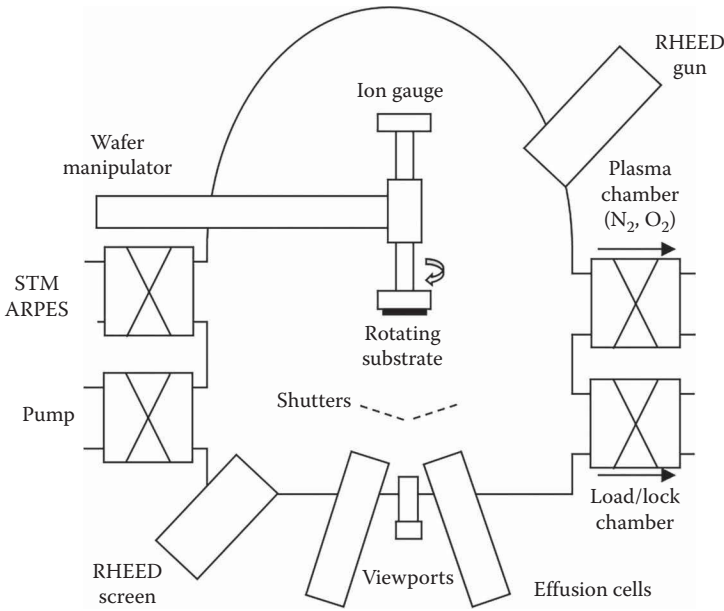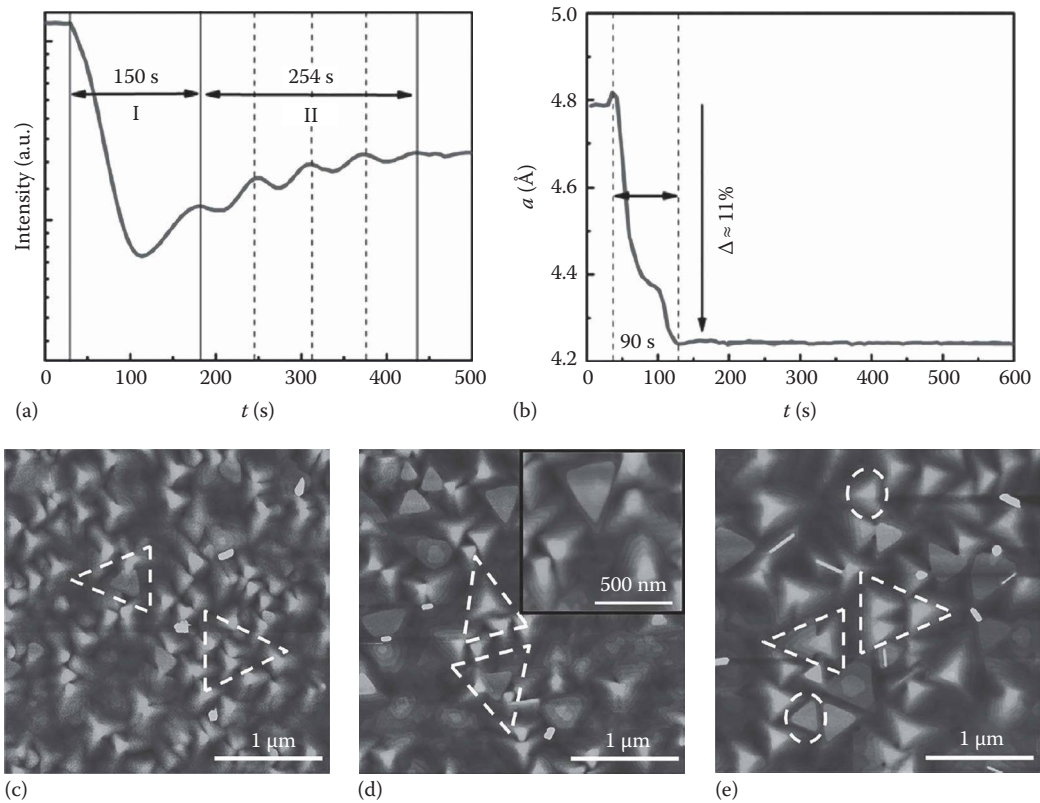
FIGURE 3.3
A schematic of a molecular beam epitaxy system.

cell and a Se- (Te-) containing cell are engaged at the same time. Heated Te often comes out of the effusion cell as a clustered molecule instead of individual atoms [115]. An additional heating filament near the opening may help to *crack* these Te clusters before they escape the effusion cell. Such a specially designed two-stage thermal cracker cell is preferred to achieve a stable and uniform Te flux. Considering that bismuth expands upon solidification, extreme care should be taken when programming the thermal cycling of Bi-cells. Sudden cooling of molten bismuth, which may break the crucible and damage the effusion cell, should be avoided at all times. Instead of using single-elemental fluxes of Sb and Te, Sb_2Te_3 seems to grow better by directly evaporating Sb_2Te_3 compound, with a properly tuned Te compensating flux to maintain the tetradymite phase. Viewports and charge-coupled device (CCD)-based cameras are used for visual examination. Computer-controlled cell shutters are installed near the opening of the cells to realize an on-/off-type of automated manipulation during film deposition. Quartz crystal monitors are helpful in monitoring the flux rate *in situ*.

Since the mean free paths of these atoms/molecules are very long under UHV, they essentially travel as a *beam* toward the substrate. The substrates (atomically smooth single crystal pieces) are mounted upside down, facing toward the incoming fluxes. Upon arrival at the cleaned/treated surface of the substrate, different species of atoms/molecules may react and crystallize. The temperature of the substrate is adjusted accordingly to promote (prohibit) the desired (unwanted) chemical reactions and reevaporation. The substrate may also be placed in a constant rotation mode during the deposition, which improves the uniformity of the film. Postgrowth annealing is sometimes needed in order to further alter the surface morphology and the crystallinity of the as-grown film. A carefully designed combination of sample-shutter/mask movement during the growth can be used to prepare SLs, wedged samples with thickness gradients, etc. All the features mentioned earlier

FIGURE 3.4
(a) Reflection high-energy electron diffraction intensity oscillation and (b) in-plane lattice parameter evolution of $BiSbTe_3$ film grown on a sapphire (0001) substrate as a function of deposition time. AFM image (3×3 µm² in area) of $BiSbTe_3$ films deposited at substrate temperatures of (c) 485 K, (d) 500 K, and (e) 515 K. Inset in (d) shows an enlarged image of Figure 3.4d. The dashed triangles mark the opposite orientation of twin domains in the molecular beam epitaxy grown $BiSbTe_3$ films. The dashed circles in (e) highlight the twin defects in the boundary area among the oppositely oriented domains. (Reprinted from *J. Cryst. Growth*, 410, Liu, W., Endicott, L., Stoica, V.A., Chi, H., Clarke, R., and Uher, C., High-quality ultra-flat $BiSbTe_3$ films grown by MBE, 23–29. Copyright 2015, with permission from Elsevier.)

coupled with an unprecedented control of the flux rate make the MBE synthesis uniquely suitable for the epitaxial thin-film growth.

The epitaxial nature of the growing film can be conveniently monitored by surface sensitive probes such as reflection high-energy electron diffraction (RHEED). An optional differential pumping system may be used to achieve the high vacuum required for energizing the RHEED electron gun. The diffraction pattern can be monitored through the CCD camera situated behind the fluorescent RHEED screen. Depending on the operation voltage of the RHEED gun, users should be aware of and protected from the hazards of potential x-ray generation. Figure 3.4a shows the temporal evolution of the RHEED intensity profile recorded for the growth of a typical $BiSbTe_3$ ternary thin film on a sapphire (0001) substrate [83]. After completing the initial QL, the RHEED intensity starts to develop an oscillating pattern with a well-defined period. Each full cycle indicates the completion of an individual QL. This is a manifestation of the QL-by-QL vdW epitaxial growth mode. Before deposition, the in-plane lattice parameter *a* deduced from

the RHEED pattern is the value of the bare sapphire (0001) substrate. When exposed to the atomic/molecular fluxes, *a* starts to decrease and quickly settles at the bulk value of the tetradymite-type structure (Figure 3.4b). Owing to the weak vdW bonding between the adjacent B[VI] atomic layers, strains originating from the lattice mismatch can thus be fully relaxed within the first QL. This implies that the requirement of lattice matching, an often difficult to satisfy criterion for high-quality epitaxial growth (e.g., in a cubic crystal system such as GaAs), is somewhat relaxed in the growth of tetradymite-type structures with vdW layers. Note, however, despite the perfectly *c*-oriented growth, one can still have stacks or twin domains in the basal plane that are misoriented by 60°, which are observed even in high-quality MBE films [78,83,110,116]. For example, using atomic force microscopy, Liu et al. have observed 60° rotated domains in as-grown BiSbTe$_3$ MBE thin films at various substrate temperatures (see Figure 3.4c through e). These twin domains may be suppressed by optimizing growth parameters to achieve a stable film growth [110,111]. Up till now, the effect of twin domains on TE transport still remains unclear due to limited reports.

Apart from the general features mentioned earlier of preferred orientation and misoriented domains, a tetradymite-type film also possesses fine microstructures at nanoscale that are important to transport processes, such as nanoprecipitates, structure modulation, dislocations, and twin grains [80,81,85,86,94,99–101,108]. Peranio et al. [85] prepared Bi$_2$Te$_3$ and Sb$_2$Te$_3$ films on SiO$_2$ substrates by a NA method utilizing a MBE chamber, where Te and Bi/Sb were first deposited in the sequence of –Te–Bi/Sb–Te–Bi/Sb–Te– at room temperature and the as-deposited films were subsequently annealed at 250°C for 2 h. The obtained Sb$_2$Te$_3$ film possessed a strong *c*-orientation, while the Bi$_2$Te$_3$ film showed no clear epitaxial growth relation between the substrate and the film. As indicated in Figure 3.5a through e, the cross section high-resolution transmission electron microscopy (HRTEM) analysis on Sb$_2$Te$_3$ showed rich nanoscale structures, such as nanograins with size of 350–650 nm and clear fringe structures due to structure modulation with a wavelength of 5–12 nm. A selected area electron diffraction (λ) analysis showed that the two strongly *c*-oriented grains enclosed an angle of 18°, inclining at an angle of up to 37° away from the film growth direction. Figure 3.5f through j shows the HRTEM analysis of Bi$_2$Te$_3$ in cross section. The Bi-rich boundary phase, the structure modulation with a wavelength of ~10 nm, and the dislocations and polycrystalline-like SAED ring pattern are evident in the studied area. In addition, the grains in this area were found to be separated by large-angle grain boundaries, and the *c*-axis of the grains deviated by an angle of 39° from the growth direction. The microstructure of tetradymite-type films was found to be strongly related to the growth conditions and compositions. First, structure modulation and twin grains are generally reported [80,94]. Second, a cation-rich boundary phase was found in coevaporated and annealed Bi$_2$Te$_3$ film at room temperature but was not observed in the Bi$_2$Te$_3$ film prepared by traditional MBE [80] or in coevaporated and annealed Sb$_2$Te$_3$ film at room temperature [85]. Other interesting results of basal-plane/nonbasal-plane twin boundary and Te-rich precipitates were observed in PLD-deposited (Bi, Sb)Te$_3$ films [94] and electric current–stressed Bi$_2$(Se, Te)$_3$ films [101].

Although the superior *ZT* in Bi$_2$Te$_3$/Sb$_2$Te$_3$ SLs was reported some 15 years ago, reproducing such Bi$_2$Te$_3$/Sb$_2$Te$_3$ SL structure was a difficult challenge that has not yet fully succeeded regardless of using NA methods or MOCVD [79,99,100,108]. A cosputtering-assisted NA technique was used to grow *p*-type Sb$_2$Te$_3$/(Bi, Sb)$_2$Te$_3$ and *n*-type Bi$_2$Te$_3$/(Bi, Sb)$_2$Te$_3$ *soft* SLs [99,100]. The film structure closest to Bi$_2$Te$_3$/Sb$_2$Te$_3$ SLs was recently reported by Hansen et al. [81] utilizing the MBE technique. These authors established that it was possible to deposit Bi$_2$Te$_3$/Sb$_2$Te$_3$ SLs on BaF$_2$ (111) substrate at a critical temperature, where
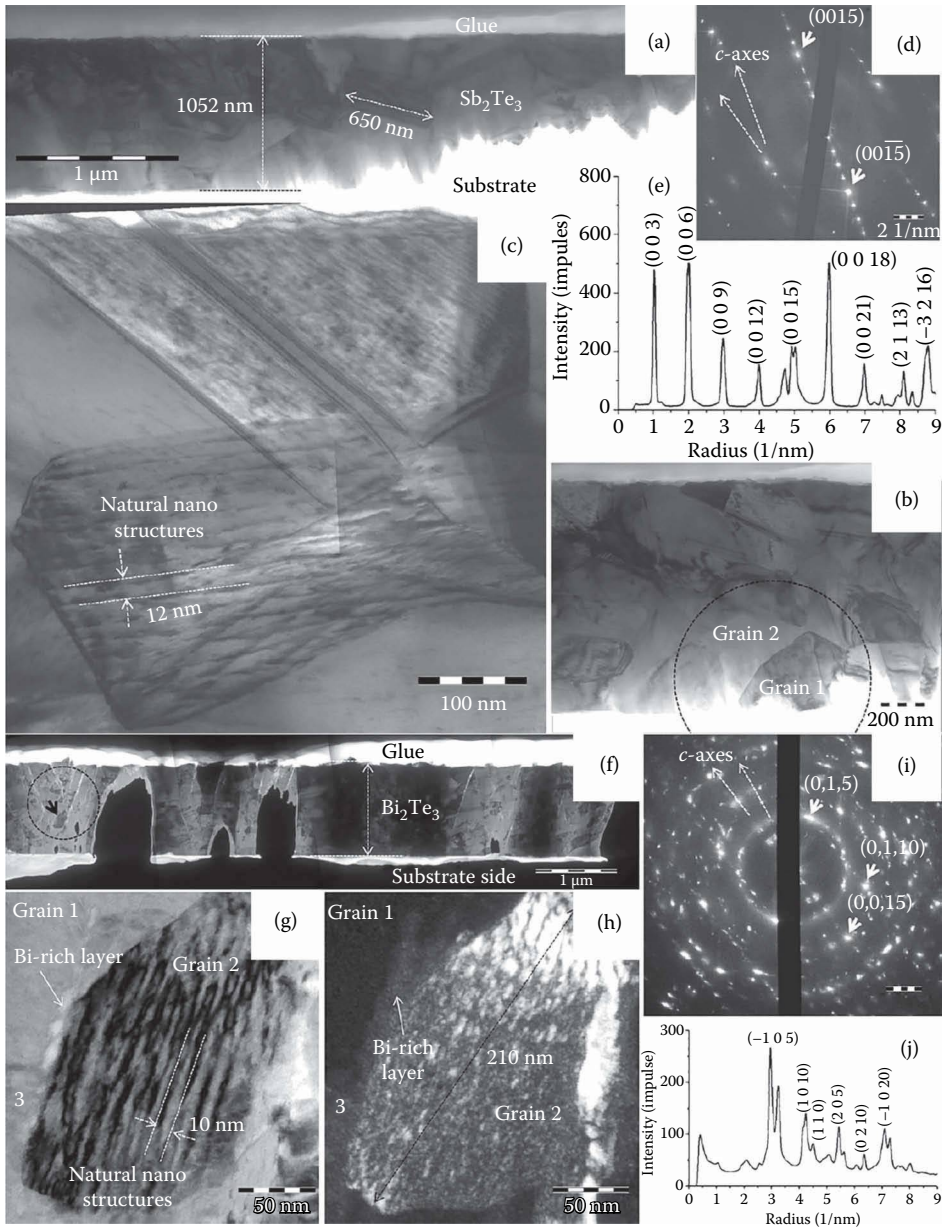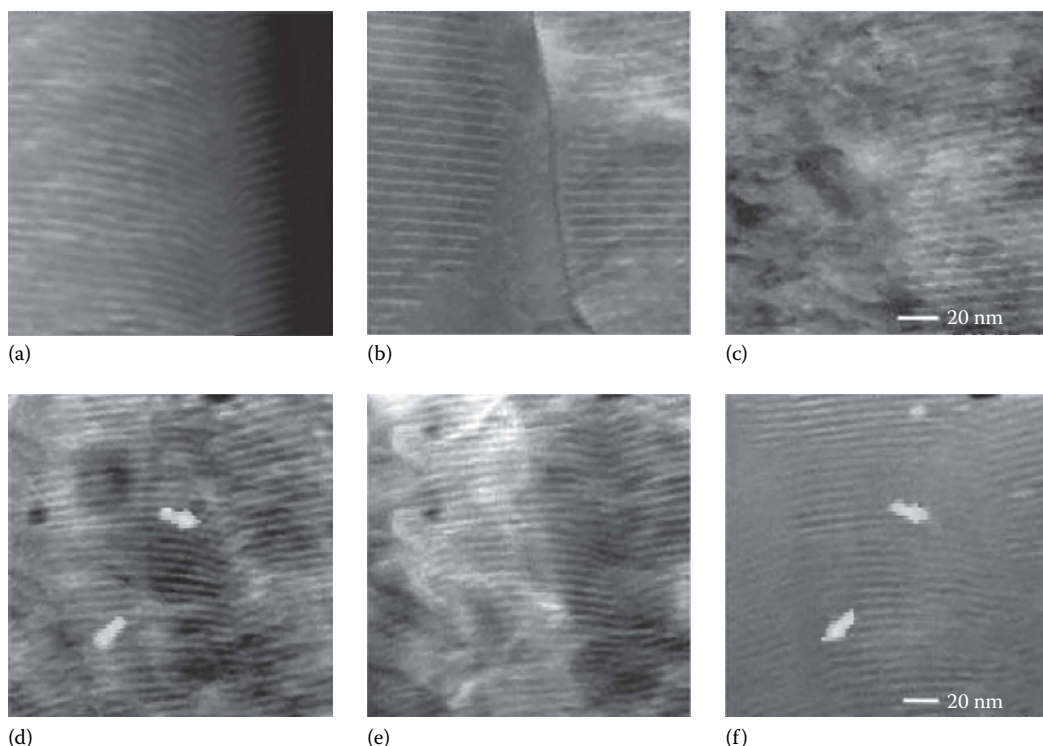
FIGURE 3.5

Transmission electron microscopy cross-sectional results obtained on the annealed (a–e) Sb_2Te_3 and (f–j) Bi_2Te_3 thin film deposited on a SiO_2 substrate. In images (a–d, f–i), the growth direction points toward the top of the images. (a) Overview of bright-field image. (b) Magnified bright-field image. (c) High-magnification bright-field image of grain boundaries. (d) Selected area electron diffraction (SAED) pattern of the encircled area in (b). (e) Normalized radial intensity profile obtained from the diffraction pattern. (f) Overview of bright-field image. (g) High-magnification bright-field image and (h) corresponding dark-field image of a grain. (i) SAED pattern obtained on the encircled area in (f). (j) Normalized radial intensity profile obtained from the diffraction pattern. (Reprinted from *J. Alloy. Compd.*, 521, Peranio, N., Winkler, M., Bessas, D. et al., Room-temperature MBE deposition, thermoelectric properties, and advanced structural characterization of binary Bi_2Te_3 and Sb_2Te_3 thin films, 163–173. Copyright 2012, with permission from Elsevier.)

the thermal energy is sufficient for the formation of SLs from evaporated elements but not high enough to trigger global interdiffusion. The optimized substrate temperature was found to be 350°C. As shown in Figure 3.6, apart from the ordered 1 nm Bi_2Te_3/5 nm Sb_2Te_3, the high-angle annular dark-field (HAADF) scanning transmission electron microscopy (STEM) analysis also identified a strongly bowed SL structure. The subsequent annealing treatments both *ex situ* and *in situ* in the transmission electron microscopy confirmed the strong fading of SL structures above 200°C. Thus, till now, SLs with ideal stacking structure do not seem to be experimentally accessible.

While 10 years ago, the growth of thin films of Bi_2Se_3, Bi_2Te_3, and Sb_2Te_3 was a specialized and rarely pursued research activity, the unprecedented boom in the study of TIs and the fact that the tetradymite-type thin-film structures are perhaps the best realization of the topological medium have resulted in widespread use of MBE growth of such thin films. As a tetradymite-type TI, Bi_2Se_3 stands out due to its large electronic gap. Additionally, its single surface Dirac cone is well defined in the band gap, far away from any interference with bulk states. These competitive advantages have drawn a tremendous attention to


(a) (b) (c)

(d) (e) (f)

FIGURE 3.6
High-angle annular dark-field (HAADF) scanning transmission electron microscopy (STEM) micrographs (the same scales) for *ex situ* heating experiments. (a) As-deposited state where strongly bowed superlattice (SL) structures are frequently observed. (b) Sample heated for 1 h at 250°C. The absence of strongly bowed SL structures is evident. (c) Further heat treatment for 1 h at 300°C led to a strong fading of the SL structure. Most of the sample showed no SL structure at all. HAADF STEM micrographs (the same scales) for *in situ* heating experiments at (d) 215°C, (e) 300°C, and (f) 360°C, respectively. Arrows mark positions with strongly bowed SL in as-deposited state. (Reprinted with permission from Hansen, A.-L., Dankwort, T., Winkler, M. et al., Synthesis and thermal instability of high-quality Bi_2Te_3/Sb_2Te_3 superlattice thin film thermoelectric, *Chem. Mater.*, 26, 6518. Copyright 2014 American Chemical Society.)

the growth of Bi_2Se_3 thin films and the topological research has much contributed to the improved quality of such films. To integrate TI/TE with the prevailing Si-based technology, the growth on Si-based substrates was clearly highly desirable, and the readily available and inexpensive Si wafer was one of the first substrates quickly tested for the growth by various groups of researchers [117–119]. An uninitiated reader might find it interesting to learn how one goes about establishing a set of optimized MBE parameters through trial and error.

In order to grow Bi_2Se_3 thin films on Si (111) substrates, earlier attempts required pre-depositing a monolayer (ML) of Bi (to form a β- $\sqrt{3} \times \sqrt{3}$ Bi surface) and/or an amorphous layer of Bi_2Se_3 at the interface [117,118]. Such intermediate layers were intended to recover the smooth Si (111) 1 × 1 surface from the somewhat rough 7 × 7 surface and improve the film crystallinity. More recently, Bansal et al. demonstrated that these interfacial layers can be dispensed of after all [119]. It turned out that the substrate temperature was the key parameter of producing high-quality Bi_2Se_3 films. To obtain an optimal surface layer that minimizes the formation of defects and secondary phases in the first place, the substrate was treated with an *ex situ* ultraviolet ozone-cleaning procedure and then heated briefly up to ~900°C in the UHV chamber. The undesired Si (111) 7 × 7 surface (Figure 3.7a)
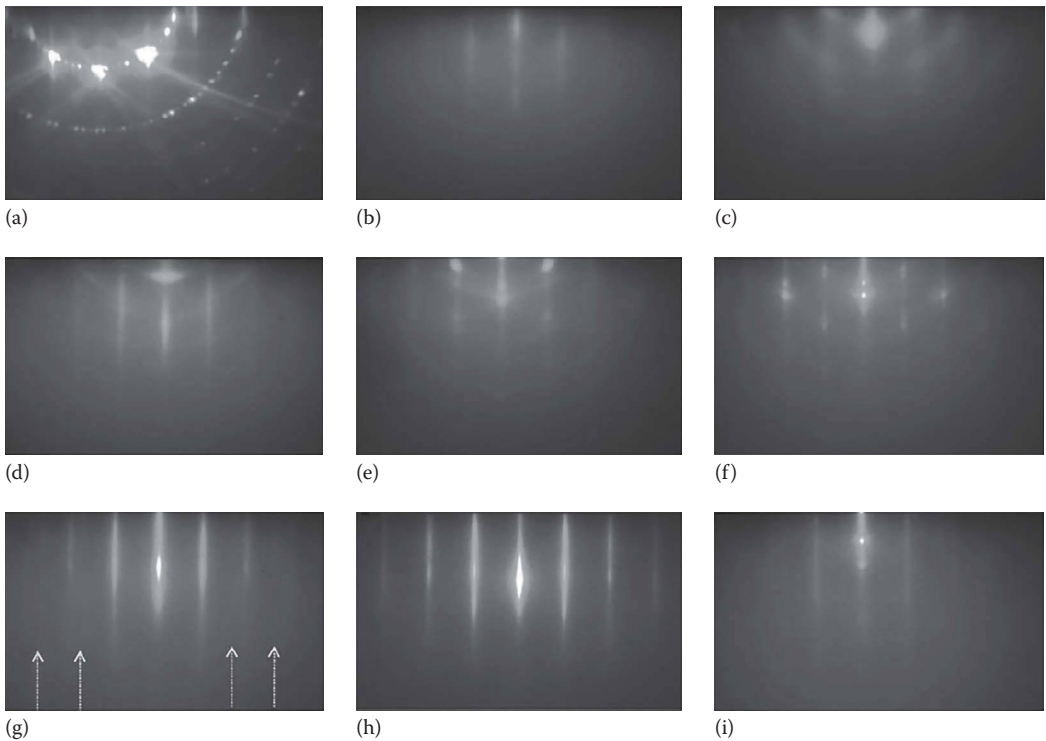
FIGURE 3.7
Reflection high-energy electron diffraction patterns of Bi_2Se_3 on Si (111) under different growth temperatures. (a) Reconstructed Si (111) 7 × 7 surface after cleaning treatment. (b) Short-term (2.5 min) and (c) long-term (10 min) low-temperature growth at 110°C. Short-term (~2.5 min) high-temperature growth at (d) 190°C, (e) 250°C, and (f) 350°C, respectively. Two-temperature growth including an initial 2–3 quintuple layer deposition at 110°C and higher temperature growth at (g) 190°C, (h) 230°C, and (i) 300°C, respectively. (Reprinted from *Thin Solid Films*, 520, Bansal, N., Kim, Y.S., Edrey, E. et al., Epitaxial growth of topological insulator Bi_2Se_3 film on Si(111) with atomically sharp interface, 224–229. Copyright 2011, with permission from Elsevier.)

was unreconstructed upon exposure to Se flux. A ML of Se was formed at ~100°C, while lower (higher) substrate temperature resulted in amorphous Se accumulation (SiSe$_2$ layers). The Se ML passivated the Si surface as well as provided a base for the stacking of the Se-terminated QL of Bi$_2$Se$_3$. Attempts of single-step growth at a fixed temperature were not satisfactory. The growth at 110°C resulted in weak streaky patterns (Figure 3.7b) suggesting that the temperature was too low to promote crystallization, while further growth at this temperature led to the formation of polycrystalline ring patterns (Figure 3.7c). Sharper streaks were obtained (Figure 3.7d) when directly grown at a higher temperature (190°C). However, the associated ringlike patterns indicated a rather disordered crystallographic orientation within the film. Further increasing the substrate temperature resulted in the formation of islands/clusters at 250°C (Figure 3.7e) or even secondary phases at 350°C (Figure 3.7f). However, when combining a low-temperature (110°C) growth of the initial 2–3 QLs (to prevent reaction with silicon substrate) and a high-temperature (230°C) growth for subsequent layers of the film (to improve crystallinity), a significantly higher quality was achieved, as demonstrated in the very sharp streaky pattern in Figure 3.7h. As illustrated in Figure 3.7g and i, there was an optimized temperature window for the high-temperature stage of the growth, as too low (high) temperature led to the formation of undesired twin structure (secondary phases).

3.4 Transport Properties

Galvanomagnetic and thermal measurements on tetradymite-type thin films are typically performed using dedicated *ex situ* experimental setups, where the control of temperature, electromagnetic fields, and thermal gradient and laser signals are readily implemented. These systems include the versatile characterization platforms such as the Magnetic Property Measurement System and Physical Property Measurement System from Quantum Design. However, caution should be used in designing experimental protocols so that contamination and oxidation of films are eliminated or at least minimized. Owing to their clear advantages, for example, in overcoming contamination or oxidation, *in situ* transport instrumentations in UHV-compatible cryostats are currently being actively pursued [110,120]. Due to the vdW epitaxial nature, the most commonly characterized electronic properties are the in-plane ($\perp c$) electrical resistivity (ρ_{xx}) and Hall resistivity (ρ_{yx}) or Hall coefficient ($R_H = \rho_{yx}/B$), which can be measured using the van der Pauw method or a Hall bar geometry. The former case requires a perfect square sample with contacts placed on the four corners. In the latter case, the electric current is fed through the outmost longitudinal contacts on a rectangular profile sample, and the resistivity voltage is probed via the inner longitudinal leads, while the Hall voltage is monitored using the transverse leads under external magnetic field. A low frequency ac current is recommended to minimize the Peltier heating effects. With a longitudinal temperature gradient established via heater/sink situated at either end of the Hall bar device, the in-plane Seebeck coefficient (α) can be obtained by probing the longitudinal voltage difference under steady-state conditions. As for measurements across the plane ($||c$), the electronic properties usually require photolithography procedures to provide the necessary length/cross section ratio. While in principle one might be able to measure the in-plane thermal conductivity by the steady-state method,

stringent criteria between film and the substrate have to be satisfied first. This makes the steady-state method practically irrelevant for the thermal conductivity measurement of thin films, unless, in the rare cases, the film can be suspended or when the film is very thick and its thermal conductivity is significantly higher than that of the substrate. The across-plane thermal conductivity can be measured by the newly developed time-domain thermoreflectance method [121,122] and the transient 3ω method [123–126]. A modification of the 3ω technique, together with 2D conduction modeling, might be adopted for the estimation of in-plane thermal conductivity. More detailed reviews on the transport measurement techniques were recently provided by Wang et al. [78] and Völklein et al. [127].

The strategies utilized so far to enhance the TE properties of tetradymite-type films have concentrated on (1) enhancing the carrier mobility via fabricating films with preferred orientation, (2) optimizing the carrier density via engineering the defect formation, and (3) reducing the lattice thermal conductivity via strengthening the phonon scattering. We herein focus on the recent progress in tuning the TE transport properties of tetradymite-type films. Specifically, the discussion of in-plane electronic properties and across-plane thermal conductivity will be emphasized.

Using the two-step MBE growth method, Bansal et al. [31] have prepared a series of single crystalline Bi_2Se_3 MBE thin films on sapphire (0001) substrates, with thicknesses ranging from 2 to 256 QLs. The superior quality of these Bi_2Se_3 thin films has allowed the authors to study the thickness-independent surface transport channels. The temperature-dependent sheet resistances $R_\square$ are shown in Figure 3.8a. Overall, these Bi_2Se_3 MBE thin films all exhibit typical metallic temperature dependence—a positive temperature coefficient of resistivity at high temperature due to electron–phonon interaction, which flattens out at the lowest temperature. Upon increasing the thickness, $R_\square$ drops rather rapidly by adding the first several QLs and then essentially saturates at and above 8 QLs. The thickness dependence is more clearly visualized in Figure 3.8b, where the conductance G_{xx} at $T = 1.5$ K is collected for all the thicknesses. These stoichiometric films possess a nonlinear magnetic field dependence of the Hall resistance, a signature of multiband conduction. Through a two-band model, the analysis identified the existence of two surface channels: a channel composed of topological SSs with carrier concentration ~3.0×10^{13} cm^{-2} (constant down to 2 QL) and another one of the surface accumulation nature with a somewhat lower carrier density ~8.0×10^{12} cm^{-2} (constant only down to ~8 QL).

Furthermore, as shown in Figure 3.8c, the magnetoresistance develops a WAL-type of cusp at low magnetic fields, which can be readily analyzed using the Hikami, Larkin, and Nagaoka (HLN) quantum interference model [128],

$$\Delta G(B) = -A \frac{e^2}{h} \left[\psi\left(\frac{\hbar}{4eL^2B} + \frac{1}{2} \right) - \ln\left(\frac{\hbar}{4eL^2B} \right) \right], \tag{3.4}$$

where ψ is the digamma function, e is the elementary charge, $\hbar$ (= $h/2\pi$) is the Planck constant, and L is the phase coherence length.

Theoretically, the fitting parameter A is predicted to be $1/2\pi$ for each 2D conduction channel (i.e., $2\pi A$ is the effective number of conduction channels). Typical values for A lie between two limiting scenarios in a thin film: (1) $1/\pi$ if the top and bottom surfaces are completely decoupled from each other by an insulating bulk and (2) $1/2\pi$ in the case where the two surfaces are coupled by the bulk or the bulk of the film dominates the conduction.
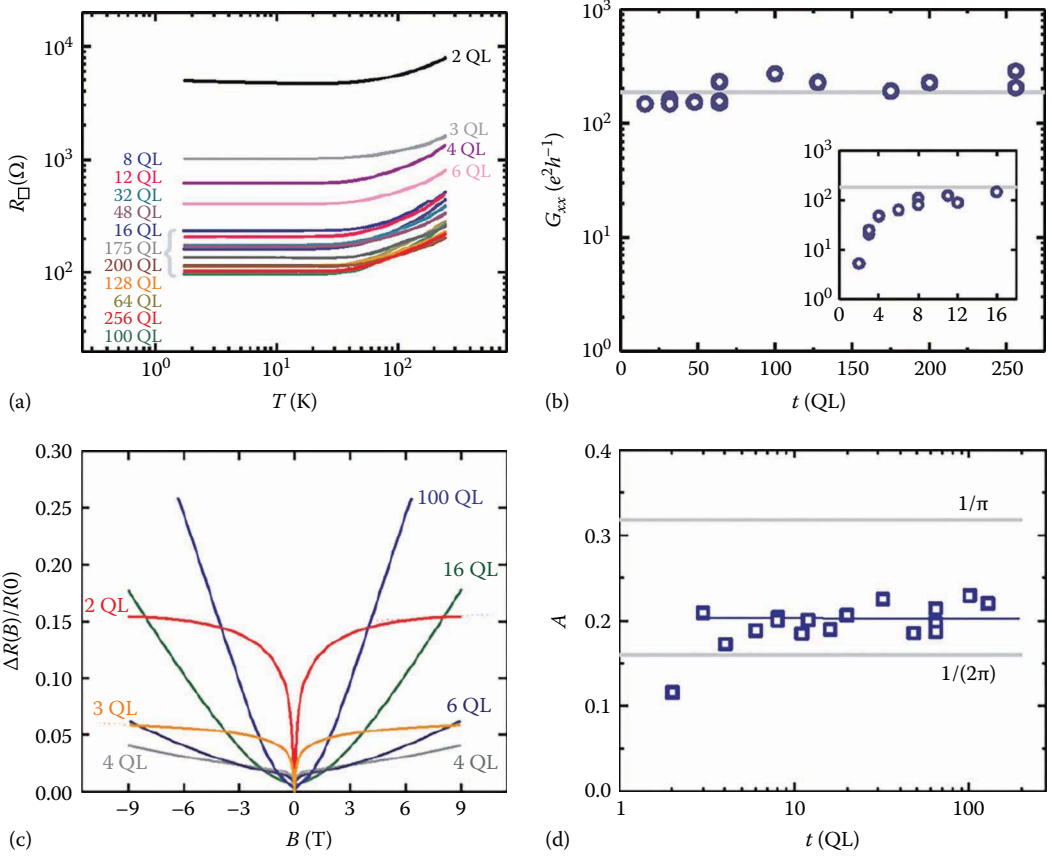
FIGURE 3.8
Transport properties of pure Bi_2Se_3 films with different thickness. (a) Temperature-dependent sheet resistance $R_\square$ at various film thickness. (b) Conductance at 1.5 K as a function of thickness. (c) The weak antilocalization effect at 1.5 K for selected thicknesses. (d) The fitting parameter A in the Hikami, Larkin, and Nagaoka quantum interference model indicating effective number of conduction channels. (Reprinted with permission from Bansal, N., Kim, Y.S., Brahlek, M., Edrey, E., and Oh, S., *Phys. Rev. Lett.*, 109, 116804, 2012. Copyright 2012 by the American Physical Society.)

The observed values of the fitting parameter A are shown in Figure 3.8b and, indeed, reside between the two limits. Nevertheless, the thickness independence of A, above 3QLs, is in agreement with the aforementioned behavior of surface conduction.

By carefully examining the WAL effects using the HLN model in Bi_2Se_3 thin films with different Cu doping and various thicknesses, see Figure 3.9a, Brahlek et al. have recently established a narrow composition window where completely decoupled surface conduction (with $A = 1/\pi$) is realized [129]. It appears that localized bulk states can be achieved in Bi_2Se_3 thin films upon fine tuning the Cu doping level (Figure 3.9b). With such Cu content, the nonlinearity of the field-dependent Hall resistance is greatly suppressed. The optimized Bi_2Se_3 thin films start to show decoupled SSs as the film thickness exceeds an intersurface coupling length (Figure 3.9c). This observation provides an important experimental route of decoupling SSs in tetradymite-type thin films via chemical doping and thickness control.
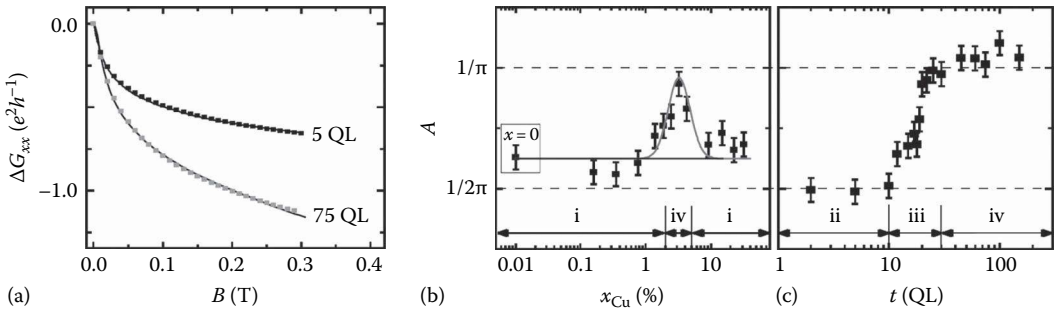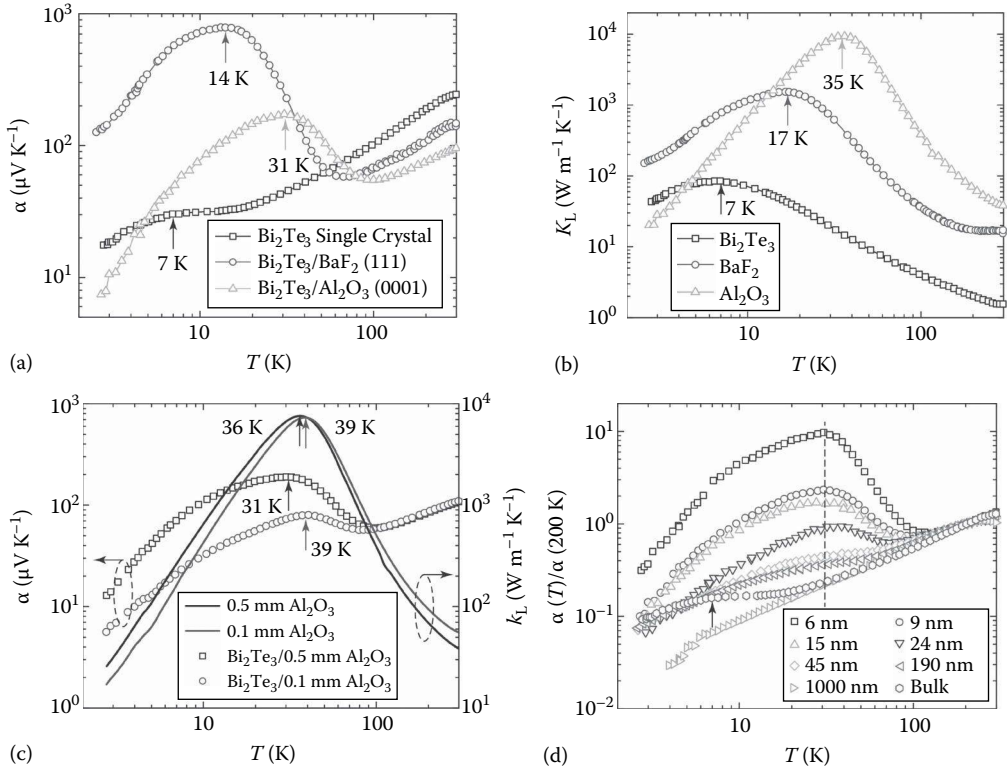
FIGURE 3.9
Weak antilocalization (WAL) effect in Cu-doped Bi_2Se_3 thin films. (a) Typical Hikami, Larkin, and Nagaoka fitting of the WAL-type cusp in conductance at low magnetic fields. Fitting parameter A, the effective number of 2D channels, as a function of (b) composition (x_{Cu}) for fixed thickness (20 QLs) and (c) thickness for fixed composition ($x_{Cu} \approx 2.5\%$–4.0%). (Reprinted with permission from Brahlek, M., Koirala, N., Salehi, M., Bansal, N., and Oh, S., *Phys. Rev. Lett.*, 113, 026801, 2014. Copyright 2014 by the American Physical Society.)

Subjected to a thermal gradient at low temperatures, the charge carrier system in a single crystal may be *dragged* by out-of-equilibrium phonons, leading to significantly enhanced values of the thermopower, the phenomenon known as the phonon-drag effect. Using Bi_2Te_3 as an example, Wang et al. have recently assessed the influence of phonons from the substrates on charge carriers in thin films [130]. As shown in Figure 3.10b, the phonon thermal conductivity of a crystal develops a dielectric peak at low temperatures. The conductivity peak position is related to the Debye temperature of the corresponding substrate/crystal—165, 282, and 980 K for Bi_2Te_3, BaF_2, and Al_2O_3, respectively. It appears that the phonons governing the lattice thermal conductivity are the same as those dominating the phonon-drag thermopower. The peak of the phonon drag (in Figure 3.10a) appears at virtually the same temperature as the peak in the phonon thermal conductivity. As shown in Figure 3.10c, reducing the thickness of the sapphire substrate enhances the grain boundary scattering at the lowest temperatures, which effectively increases the peak temperature of the phonon conductivity (solid lines). This subtle increase also seems to push the phonon-drag peak position to slightly higher temperatures. Figure 3.10d suggests that the influence from substrate phonons diminishes quickly upon increasing the film thickness, and eventually, the bulk value should be restored. These experimental features demonstrate the researchers' capability to tune the position and magnitude of the phonon-drag peak over a large temperature range by simply depositing tetradymite-type thin films on substrates with different Debye temperatures.

Recently, Zhang et al. have grown a series of Bi_2Te_3–Sb_2Te_3 solid solution ultrathin films with 5 QL thickness [131]. As shown in Figure 3.11a, with high Sb content, these $(Bi_{1-x}Sb_x)_2Te_3$ films exhibit somewhat nonmetallic sheet resistance profile. Upon increasing the Sb content x, an n-to-p transition occurs in between $x = 0.90$ and 0.95, according to the Hall coefficient measurement (Figure 3.11b). As shown in Figure 3.11c, due to the bipolar excitation across the bulk band gap, the Seebeck coefficient changes sign near ambient temperature, even for relatively low Sb substitution $x = 0.70$–0.80. In particular, for $x = 0.90$, over the whole temperature range, the Hall coefficient (negative) and the Seebeck coefficient (positive) take different signs, a signature of multiband conduction. Considering that these films are extremely thin, SSs might, indeed, be playing a role in the transport. The possibility and feasibility of developing TE devices utilizing TI concepts have been discussed [132–134].

FIGURE 3.10

(a) Temperature-dependent thermopower for Bi_2Te_3 single crystal, 9 nm Bi_2Te_3 films on BaF_2 (111), and sapphire (0001) substrates. (b) The lattice thermal conductivity of Bi_2Te_3 single crystal, bare BaF_2 and sapphire substrates. (c) Thermopower of two 9 nm films grown on sapphire substrates with different thicknesses. The lattice thermal conductivities (right axis) of two substrates are also shown. (d) Normalized thermopower (to the value at 200 K) for Bi_2Te_3 single crystal and films with different thickness on sapphire substrate. (Reprinted with permission from Wang, G., Endicott, L., Chi, H., Lošt'ák, P., and Uher, C., *Phys. Rev. Lett.*, 111, 046803, 2013. Copyright 2013 by the American Physical Society.)

The anisotropic nature of tetradymite-type structure dictates that *c*-oriented films have superior TE performance [135,136]. The room temperature electronic transport properties of binary Bi_2Te_3 and Sb_2Te_3 films grown using various techniques are summarized in Table 3.4. Bi_2Te_3 and Sb_2Te_3 films with stronger (00*l*) orientation indeed possess a much larger carrier mobility. The carrier mobility of the (015)-oriented Bi_2Te_3 and Sb_2Te_3 films are only about 20 cm^2 V^{-1} s^{-1}, which is at least twice smaller than that of (00*l*)-orientated films [103,104]. For the Bi_2Te_3 with high electron density of 6.5–12 × 10^{19} cm^{-3}, it is evident that the (00*l*)-orientated Bi_2Te_3 films possess much higher Seebeck coefficient than the (015)-oriented films, which is likely due to the anisotropy in the Seebeck coefficient [56,103]. Thus, the (00*l*)-oriented Bi_2Te_3 and Sb_2Te_3 films possess an excellent power factor of 4.0 and 3.1 mW m^{-1} K^{-2} due to their preferred orientation [56,104]. A similar trend has also been observed in Bi_2Se_3 or ternary tetradymite-type films [66,75,82,85]. As compared to the bulk single crystal counterparts, the carrier mobility obtained in films is still low, especially for the *n*-type Bi_2Te_3 films, and the carrier density is not at an optimal value. Therefore, the improvement in the film orientation and the optimization of carrier density
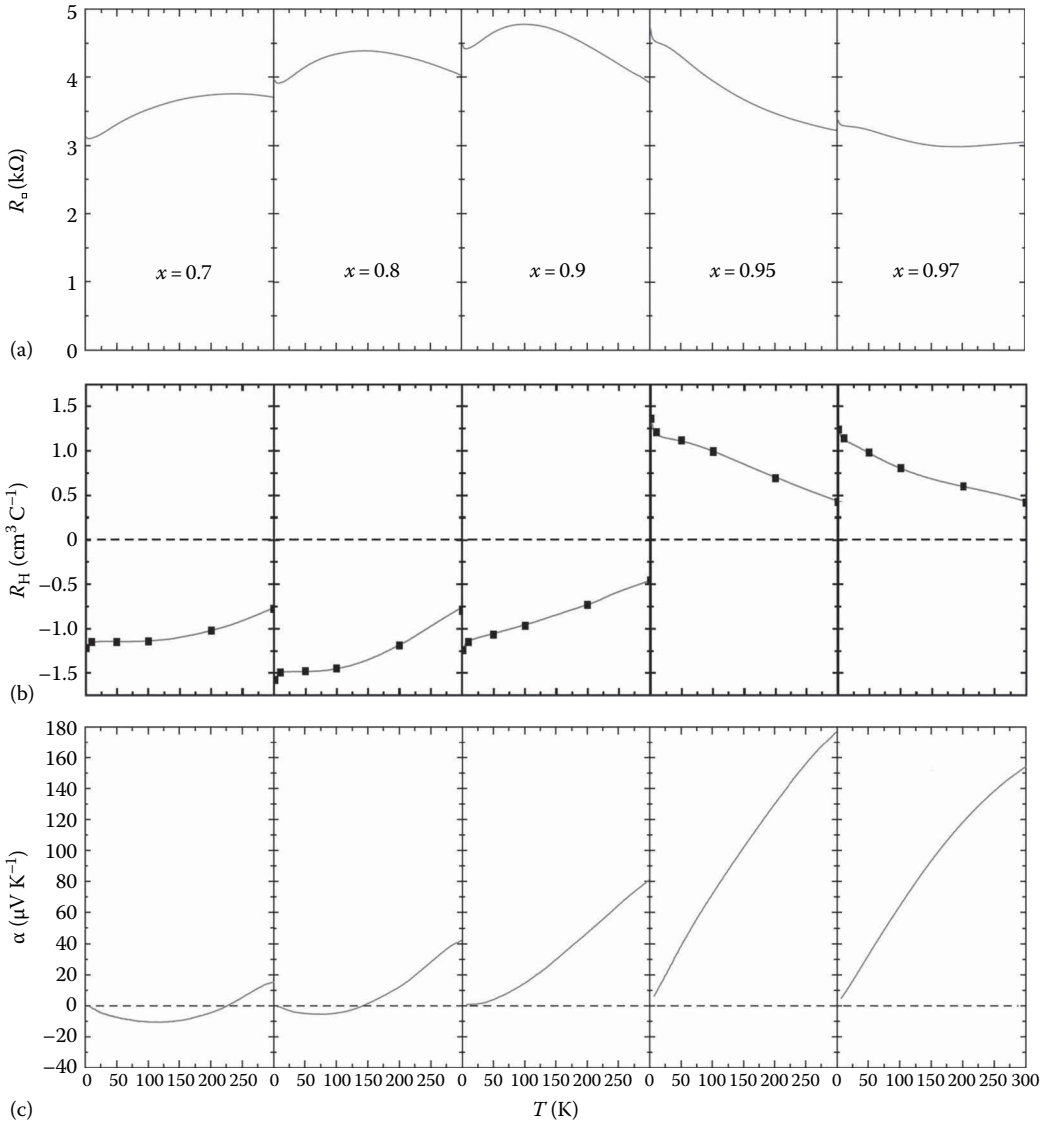
FIGURE 3.11
The (a) sheet resistance, (b) Hall coefficient, and (c) Seebeck coefficient of 5 quintuple layer $(Bi_{1-x}Sb_x)_2Te_3$ films. (Reprinted with permission from Zhang, J., Feng, X., Xu, Y. et al., *Phys. Rev. B*, 91, 075431, 2015. Copyright 2015 by the American Physical Society.)

are still needed to achieve a further improved power factor in tetradymite-type films. In order to strengthen phonon scattering and reduce lattice thermal conductivity, reducing grain size and increasing boundary density are two widely accepted experimental routes [8,13,137]. In tetradymite-type films, decreasing the grain size and forming SL structures are considered to be the most effective approach to reduce the lattice thermal conductivity, while the effect from structure modulation and film thickness is also included in the discussion of grain size effect.

TABLE 3.4

Room Temperature In-Plane Electronic Transport Properties of Binary Bi_2Te_3 and Sb_2Te_3 Films

Methods	Reference	Materials	Orientation	n	μ	σ	α	PF
Nanoalloying	[85]	Bi_2Te_3	$(00l) + (10\bar{1}1)$	2.7	62	2.7	−182	0.9
		Bi_2Te_3	$(00l) + (10\bar{1}1)$	2.7	79	3.4	−153	0.8
		Sb_2Te_3	$(00l) + (10\bar{1}1)$	2.8	430	19.3	125	3.0
		Sb_2Te_3	$(00l) + (10\bar{1}1)$	2.6	408	17	130	2.9
Sputtering	[103]	Bi_2Te_3	(015)	12	22	4.3	−122	0.6
			$(00l)$	10	52	8.4	−200	3.4
Sputtering	[104]	Sb_2Te_3	(015)	9.1	19	2.8	175	0.9
			$(00l)$	4.2	100	6.7	214	3.1
Thermal evaporation	[54]	Bi_2Te_3	$(00l) + (015)$	3.1	107	5.3	−208	2.3
		Sb_2Te_3	$(00l)$	1.4	348	7.8	160	2.0
Thermal evaporation	[56]	Bi_2Te_3	$(00l) + (110)$	6.5	74	7.7	−228	4.0
		Sb_2Te_3	$(00l)$	3.4	176	9.6	171	2.8

Carrier density, n (10^{19} cm^{-3}); mobility, μ (cm^2 V^{-1} s^{-1}); electrical conductivity, σ (10^4 S m^{-1}); Seebeck coefficient, α (μV K^{-1}); power factor, $PF \equiv \alpha^2\sigma$ (10^{-3} W m^{-1} K^{-2}).

It is well accepted that the transport properties of tetradymite-type films are dominated by native point defects such as antisite defects and vacancies, due to their low formation energy. The carrier density of tetradymite-type films grown under out-of-equilibrium conditions may vary in the range of 10^{18}–10^{21} cm^{-3} depending on the material and growth parameters. Varying the ratio of B^{VI}/A^V species during the deposition or adding a postannealing process can modify the carrier density of tetradymite-type films. In single crystals, increasing the B^{VI}/A^V ratio increases the electron density of Bi_2Te_3 and decreases the hole density of Sb_2Te_3 due to the increasing amount of Te [2]. However, this is not the case in the thin films [73,75,76]. For example, the electron density of Bi_2Te_3 film decreases by one order of magnitude when the Te/Bi ratio increases from 3 to 9 [76], while the hole density of Sb_2Te_3 film increases by 25% when Te/Sb ratio increases from 5 to 7 [73]. These results suggest further efforts are still needed to clarify the different effects of the B^{VI}/A^V ratio in bulk crystals and thin films. Postannealing is commonly used to promote the crystallinity and to tune the carrier density of as-deposited films [85]. Postannealing at elevated temperatures, commonly not higher than 300°C, tends to decrease the electron density of n-type films of Bi_2Te_3 [82,85] and Bi_2(Te, Se)$_3$ [66]. Annealing in a Te-rich environment follows the same trend [106]. In contrast, annealing in p-type films is mostly reported to increase the hole density, as observed in (Bi, Sb)$_2$Te$_3$ [82,85] films and Sb_2Te_3/(Bi, Sb)$_2$Te$_3$ SLs [99]. This is usually explained by the Te reevaporation and the creation of (Bi, Sb)$_{Te}$ antisite defects, which generate hole carriers in films.

The thermal conductivity data of selected tetradymite-type films are collected in Table 3.5. Upon decreasing the grain size or film thickness of tetradymite-type films, the across-plane thermal conductivity can be largely reduced. As reported by Chiritescu et al. [138] and Takashiri et al. [139], the across-plane thermal conductivity of the c-oriented Bi_2Te_3 film with thickness of 30–150 nm was in the range of 0.55–0.75 W m^{-1} K^{-1}, significantly lower than that of bulk single crystalline Bi_2Te_3. A similar reduction was also observed in 50 nm thick $BiSbTe_3$ films [138]. In contrast, $(Bi_{1-x}Sb_x)_2Te_3$ films, with $x = 0.20$, 0.25, and 0.35 and a grain size of several hundred nanometer, possessed a rather high κ value of ~1.0 W m^{-1} K^{-1}, close to that of their bulk counterparts (0.70–0.88 W m^{-1} K^{-1}) [2,94].

TABLE 3.5

The Film Thickness t (nm), Grain Size or Superlattice Period Δ (nm), and Room Temperature Thermal Conductivity κ (W m^{-1} K^{-1}) or Lattice Thermal Conductivity κ_L (W m^{-1} K^{-1})

Method	Reference	Materials	t	Δ	κ or κ_L	
MOCVD	[19]	Bi_2Te_3/Sb_2Te_3 SL	400–700	5	κ_L, 0.22	Across-plane
			400–700	6	κ_L, 0.25	Across-plane
MBE	[80]	Bi_2Te_3	1000	—	κ, 1.87; κ_L, 1.48	In-plane
		Bi_2Te_3/Sb_2Te_3 SL	1000	10	κ, 1.25; κ_L, 1.01	In-plane
CE	[138]	Bi_2Te_3	30–100	—	κ, 0.55–0.75	Across-plane
		$BiSbTe_3$	50	—	κ, 0.36	Across-plane
FE	[139]	Bi_2Te_3	200	150	κ, 0.6	Across-plane
NA	[100]	$Bi_2Te_3/(Bi_{0.9}Sb_{0.1})_2Te_3$	1500	50	κ_L, 0.53	Across-plane
			1500	50	κ_L, 0.79	Across-plane
NA	[99]	$Sb_2Te_3/(Bi_{0.2}Sb_{0.8})_2Te_3$	1500	50	κ, 0.45	Across-plane
PLD	[94]	$Bi_{0.4}Sb_{1.6}Te_3$	490	—	κ, 1.10	Across-plane
		$Bi_{0.5}Sb_{1.5}Te_3$	690	—	κ, 0.97	Across-plane
		$Bi_{0.7}Sb_{1.3}Te_3$	1250	—	κ, 1.00	Across-plane
MBE	[108]	Bi_2Te_3/Sb_2Te_3 SL	996	6	κ, 0.60; κ_L, 0.28	Across-plane

The thermal conductivity of SLs was obviously lower than that of the nanostructured films, as observed in Bi_2Te_3/Sb_2Te_3 SLs with SL period of 4–6 nm and low lattice thermal conductivity of 0.22–0.25 W m^{-1} K^{-1} [140]. Winkler et al. succeeded in fabricating the 1 nm Bi_2Te_3/5nm Sb_2Te_3 SL film with good crystallinity utilizing a modified MBE process [108], which, probably for the first time, came very close to reproducing the superb ZT values of the Bi_2Te_3/Sb_2Te_3 SL structure [19]. The lattice thermal conductivity of this Bi_2Te_3/Sb_2Te_3 SL film was estimated to be 0.28 W m^{-1} K^{-1} assuming a Lorenz number $L = 2.45 \times 10^{-8}$ V^2 K^{-2} and conductivity anisotropy ratio of 1.12. This was very close to the previously reported value of 0.25 W m^{-1} K^{-1} [19]. p-Type $Sb_2Te_3/(Bi_{0.2}Sb_{0.8})_2Te_3$ and n-type $Bi_2Te_3/(Bi_{0.9}Sb_{0.1})_2Te_3$ *soft* SL structured films prepared by the NA technique were also examined by Winkler et al. [99,100]. Their thermal conductivity was ~0.5 W m^{-1} K^{-1}, which was similar to the values reported in nanostructured films. Therefore, in order to improve TE performance, the tetradymite-type films should combine SL structure (effectively reduced lattice thermal conductivity) with excellent crystallinity (good electronic performance). In addition to the reports in across-plane thermal conductivity, there were also several reports on the in-plane thermal conductivity of tetradymite-type films by Peranio et al. [80] and Tan et al. [57], which considered Bi_2Te_3, Bi_2Te_3/Sb_2Te_3 SL and Sb_2Te_3 films. These results showed that the in-plane thermal conductivity was largely reduced compared to the bulk materials, as a result of the additional phonon scattering from reduced grain size.

In spite of this progress, several issues still remain unclear. First, in contrast to the very high Seebeck coefficient $\alpha \sim$ 200–270 μV K^{-1} and mobility $\mu \sim$ 600 cm^2 V^{-1} s^{-1} in MOCVD-grown SLs, the MBE-grown SLs possess a much smaller value of $\alpha \sim$ 120 μV K^{-1} and $\mu \sim$ 60 cm^2 V^{-1} s^{-1} [19,108]. Likely, the carrier density in the SL was not optimized, or there was a significant effect from minority carriers at room temperature. Alternatively, this might be caused by the compensation effect in the electronic transport from n-type Bi_2Te_3 component layer and p-type Sb_2Te_3 layer. Second, the interdiffusion of component layers in SLs during deposition is still controversial [81,141]. Third, the reported anisotropy of

SL structures remains as a surprise in that the across-plane electrical conductivity is very close to, or even larger than, the in-plane values [19,108]. Therefore, systematic investigations of carrier density optimization, controllable growth of SLs and their thermal stability, and TE property characterization in both the in-plane and across-plane orientations, as well as full-scale microstructure characterization, are still needed. These issues are crucial for future Peltier cooling applications of tetradymite-type films.

3.5 Conclusion

Tetradymite-type thin films and SLs are gaining considerable research interest worldwide as promising TEs. We have summarized their material structure and fabrication techniques, along with their transport properties. While lacking behind the bulk TE development, tetradymite-type thin-film TEs hold promise through improving the film quality and developing reliable ways of reducing their thermal conductivity. No doubt, the most recent enthusiasm in tetradymite-based TI thin-film structures will be an added impetus for further study and development of tetradymite-type thin films and SLs.

Acknowledgment

References

1. Goldsmid, H. J. and R. W. Douglas. 1954. The use of semiconductors in thermoelectric refrigeration. *Br. J. Appl. Phys.* 5: 386.
2. Rowe, D. M., ed. 1995. *CRC Handbook of Thermoelectrics*. Boca Raton, FL: CRC Press.
3. Rowe, D. M., ed. 2006. *Thermoelectrics Handbook: Macro to Nano*. Boca Raton, FL: CRC Press.
4. Yang, J. H., H. L. Yip, and A. K. Y. Jen. 2013. Rational design of advanced thermoelectric materials. *Adv. Energy Mater.* 3: 549–565.
5. Zhang, Q. H., X. Y. Huang, S. Q. Bai, X. Shi, C. Uher, and L. D. Chen. 2016. Thermoelectric devices for power generation: Recent progress and future challenges. *Adv. Eng. Mater.* 18: 194–213.
6. Borup, K. A., J. de Boor, H. Wang et al. 2015. Measuring thermoelectric transport properties of materials. *Energy Environ. Sci.* 8: 423–435.
7. Poudel, B., Q. Hao, Y. Ma et al. 2008. High-thermoelectric performance of nanostructured bismuth antimony telluride bulk alloys. *Science* 320: 634–638.
8. Xie, W., J. He, H. J. Kang et al. 2010. Identifying the specific nanostructures responsible for the high thermoelectric performance of (Bi, Sb)$_2$Te$_3$ nanocomposites. *Nano Lett.* 10: 3283–3289.

9. Kim, S. I., K. H. Lee, H. A. Mun et al. 2015. Dense dislocation arrays embedded in grain boundaries for high-performance bulk thermoelectrics. *Science* 348: 109–114.

10. Hicks, L. D. and M. S. Dresselhaus. 1993. Effect of quantum-well structures on the thermoelectric figure of merit. *Phys. Rev. B* 47: 12727–12731.

11. Hicks, L. D. and M. S. Dresselhaus. 1993. Thermoelectric figure of merit of a one-dimensional conductor. *Phys. Rev. B* 47: 16631–16634.

12. Dresselhaus, M. S., G. Chen, M. Y. Tang et al. 2007. New directions for low-dimensional thermoelectric materials. *Adv. Mater.* 19: 1043–1053.

13. Biswas, K., J. He, I. D. Blum et al. 2012. High-performance bulk thermoelectrics with all-scale hierarchical architectures. *Nature* 489: 414–418.

14. Heremans, J. P., V. Jovovic, E. S. Toberer et al. 2008. Enhancement of thermoelectric efficiency in PbTe by distortion of the electronic density of states. *Science* 321: 554–557.

15. Heremans, J. P., Ch. M. Thrush, and D. T. Morelli. 2005. Thermopower enhancement in PbTe with Pb precipitates. *J. Appl. Phys.* 98: 063703.

16. Zebarjadi, M., G. Joshi, G. Zhu et al. 2011. Power factor enhancement by modulation doping in bulk nanocomposites. *Nano Lett.* 11: 2225–2230.

17. Faleev, S. V. and F. Léonard. 2008. Theory of enhancement of thermoelectric properties of materials with nanoinclusions. *Phys. Rev. B* 77: 214304.

18. Zhao, L.-D., G. Tan, S. Hao et al. 2016. Ultrahigh power factor and thermoelectric performance in hole-doped single-crystal SnSe. *Science* 351: 141–144.

19. Venkatasubramanian, R., E. Siivola, T. Colpitts, and B. O'Quinn. 2001. Thin-film thermoelectric devices with high room-temperature figures of merit. *Nature* 413: 597–602.

20. Peranio, N., M. Winkler, M. Dürrschnabel, J. König, and O. Eibl. 2013. Assessing antisite defect and impurity concentrations in Bi_2Te_3 based thin films by high-accuracy chemical analysis. *Adv. Funct. Mater.* 23: 4969–4976.

21. Zhang, H., C.-X. Liu, X.-L. Qi, X. Dai, Z. Fang, and S.-C. Zhang. 2009. Topological insulators in Bi_2Se_3, Bi_2Te_3 and Sb_2Te_3 with a single Dirac cone on the surface. *Nat. Phys.* 5: 438–442.

22. Chen, Y. L., J. G. Analytis, J.-H. Chu et al. 2009. Experimental realization of a three-dimensional topological insulator, Bi_2Te_3. *Science* 325: 178–181.

23. Xia, Y., D. Qian, D. Hsieh et al. 2009. Observation of a large-gap topological-insulator class with a single Dirac cone on the surface. *Nat. Phys.* 5: 398–402.

24. Hsieh, D., Y. Xia, D. Qian et al. 2009. A tunable topological insulator in the spin helical Dirac transport regime. *Nature* 460: 1101–1105.

25. Moore, J. E. 2010. The birth of topological insulators. *Nature* 464: 194–198.

26. Hasan, M. Z. and C. L. Kane. 2010. Colloquium: Topological insulators. *Rev. Mod. Phys.* 82: 3045–3067.

27. Qi, X.-L. and S.-C. Zhang. 2011. Topological insulators and superconductors. *Rev. Mod. Phys.* 83: 1057–1110.

28. Qu, D.-X., Y. S. Hor, J. Xiong, R. J. Cava, and N. P. Ong. 2010. Quantum oscillations and Hall anomaly of surface states in the topological insulator Bi_2Te_3. *Science* 329: 821–824.

29. Qu, D.-X., Y. S. Hor, and R. J. Cava. 2012. Quantum oscillations in magnetothermopower measurements of the topological insulator Bi_2Te_3. *Phys. Rev. Lett.* 109: 246602.

30. Shekhar, Ch., C. E. ViolBarbosa, B. Yan et al. 2014. Evidence of surface transport and weak antilocalization in a single crystal of the $BiTe_2Se$ topological insulator. *Phys. Rev. B* 90: 165140.

31. Bansal, N., Y. S. Kim, M. Brahlek, E. Edrey, and S. Oh. 2012. Thickness-independent transport channels in topological insulator Bi_2Se_3 thin films. *Phys. Rev. Lett.* 109: 116804.

32. He, H.-T., G. Wang, T. Zhang et al. 2011. Impurity effect on weak antilocalization in the topological insulator Bi_2Te_3. *Phys. Rev. Lett.* 106: 166805.

33. Analytis, J. G., R. D. McDonald, S. C. Riggs, J.-H. Chu, G. S. Boebinger, and I. R. Fisher. 2010. Two-dimensional surface state in the quantum limit of a topological insulator. *Nat. Phys.* 6: 960–964.

34. Hahn, T., ed. 2005. *International Tables for Crystallography, Volume A: Space-Group Symmetry.* Dordrecht, the Netherlands: Springer.

35. Pérez, V. C., J. L. Tirado, K. Adouby, J. C. Jumas, A. Abba Touré, and G. Kra. 1999. X-ray diffraction and ^{119}Sn Mössbauer spectroscopy study of a new phase in the Bi$_2$Se$_3$–SnSe system: SnBi$_4$Se$_7$. *Inorg. Chem.* 38: 2131–2135.

36. Atuchin, V. V., T. A. Gavrilova, K. A. Kokh, N. V. Kuratieva, N. V. Pervukhina, and N. V. Surovtsev. 2012. Structural and vibrational properties of PVT grown Bi$_2$Te$_3$ microcrystals. *Solid State Commun.* 152: 1119–1122.

37. Kokh, K. A., V. V. Atuchin, T. A. Gavrilova, N. V. Kuratieva, N. V. Pervukhina, and N. V. Surovtsev. 2014. Microstructural and vibrational properties of PVT grown Sb$_2$Te$_3$ crystals. *Solid State Commun.* 177: 16–19.

38. Bland, J. A. and S. J. Basinski. 1961. The crystal structure of Bi$_2$Te$_2$Se. *Can. J. Phys.* 39: 1040–1043.

39. Bindi, L. and C. Cipriani. 2004. The crystal structure of skippenite, Bi$_2$Se$_2$Te, from the Kochkar deposit, Southern Urals, Russian Federation. *Can. Mineral.* 42: 835–840.

40. Ji, H., J. M. Allred, M. K. Fuccillo et al. 2012. Bi$_2$Te$_{1.6}$S$_{1.4}$: A topological insulator in the tetradymite family. *Phys. Rev. B* 85: 201103.

41. Ivanova, L. D. and Y. V. Granatkina. 1993. Thermoelectric properties of single crystals of the Bi$_2$Te$_3$–Sb$_2$Te$_3$–Bi$_2$Se$_3$ system. *Inorg. Mater.* 29: 182–186.

42. Lundegaard, L. F., E. Makovicky, T. Boffa-Ballaran, and T. Balic-Zunic. 2005. Crystal structure and cation lone electron pair activity of Bi$_2$S$_3$ between 0 and 10 GPa. *Phys. Chem. Miner.* 32: 578–584.

43. Tideswell, N. W., F. H. Kruse, and J. D. McCullough. 1957. The crystal structure of antimony selenide, Sb$_2$Se$_3$. *Acta Crystallogr.* 10: 99–102.

44. Lundegaard, L. F., R. Miletich, T. Balic-Zunic, and E. Makovicky. 2003. Equation of state and crystal structure of Sb$_2$S$_3$ between 0 and 10 GPa. *Phys. Chem. Miner.* 30: 463–468.

45. Cucka, P. and C. S. Barrett. 1962. The crystal structure of Bi and of solid solutions of Pb, Sn, Sb and Te in Bi. *Acta Crystallogr.* 15: 865–872.

46. Barrett, C. S., P. Cucka, and K. Haefner. 1963. The crystal structure of antimony at 4.2, 78 and 298°K. *Acta Crystallogr.* 16: 451–453.

47. Adenis, C., V. Langer, and O. Lindqvist. 1989. Reinvestigation of the structure of tellurium. *Acta Crystallogr. C* 45: 941–942.

48. Keller, R., W. B. Holzapfel, and H. Schulz. 1977. Effect of pressure on the atom positions in Se and Te. *Phys. Rev. B* 16: 4404–4412.

49. Rettig, S. J. and J. Trotter. 1987. Refinement of the structure of orthorhombic sulfur, α-S$_8$ *Acta Crystallogr. C* 43: 2260–2262.

50. Rothe, K., M. Stordeur, and H. S. Leipner. 2010. Power factor anisotropy of *p*-type and *n*-type conductive thermoelectric Bi–Sb–Te thin films. *J. Electron. Mater.* 39: 1395–1398.

51. Navrátil, J., J. Horák, T. Plecháček et al. 2004. Conduction band splitting and transport properties of Bi$_2$Se$_3$. *J. Solid State Chem.* 177: 1704–1712.

52. Chi, H., W. Liu, K. Sun et al. 2013. Low-temperature transport properties of Tl-doped Bi$_2$Te$_3$ single crystals. *Phys. Rev. B* 88: 045202–045207.

53. Drasar, C., M. Steinhart, P. Lostak, H. K. Shin, J. S. Dyck, and C. Uher. 2005. Transport coefficients of titanium-doped Sb$_2$Te$_3$ single crystals. *J. Solid State Chem.* 178: 1301–1307.

54. Huang, B., Ch. Lawrence, A. Gross et al. 2008. Low-temperature characterization and micropatterning of coevaporated Bi$_2$Te$_3$ and Sb$_2$Te$_3$ films. *J. Appl. Phys.* 104: 113710.

55. da Silva, L. W., M. Kaviany, and C. Uher. 2005. Thermoelectric performance of films in the bismuth-tellurium and antimony-tellurium systems. *J. Appl. Phys.* 97: 114903.

56. Zou, H., D. M. Rowe, and S. G. K. Williams. 2002. Peltier effect in a co-evaporated Sb$_2$Te$_3$(P)–Bi$_2$Te$_3$(N) thin film thermocouple. *Thin Solid Films* 408: 270–274.

57. Tan, M., Y. Wang, Y. Deng et al. 2011. Oriented growth of A$_2$Te$_3$ (A = Sb, Bi) films and their devices with enhanced thermoelectric performance. *Sens. Actuators A Phys.* 171: 252–259.

58. Sun, Z., S. Liufu, X. Chen, and L. D. Chen. 2011. Tellurization: An alternative strategy to construct thermoelectric Bi$_2$Te$_3$ films. *J. Phys. Chem. C* 115: 16167–16171.

59. Lim, S.-K., M.-Y. Kim, and T.-S. Oh. 2009. Thermoelectric properties of the bismuth–antimony–telluride and the antimony–telluride films processed by electrodeposition for micro-device applications. *Thin Solid Films* 517: 4199–4203.

60. Schumacher, Ch., K. G. Reinsberg, R. Rostek et al. 2013. Optimizations of pulsed plated *p* and *n*-type Bi_2Te_3-based ternary compounds by annealing in different ambient atmospheres. *Adv. Energy Mater.* 3: 95–104.

61. Sun, Z., S. Liufu, X. Chen, and L.-D. Chen. 2010. Enhancing thermoelectric performance of bismuth selenide films by constructing a double-layer nanostructure. *Cryst. Eng. Commun.* 12: 2672–2674.

62. Zhu, W., J.-Y. Yang, D.-X. Zhou, C.-J. Xiao, and X.-K. Duan. 2008. Electrochemical aspects and structure characterization of VA-VIA compound semiconductor Bi_2Te_3/Sb_2Te_3 superlattice thin films via electrochemical atomic layer epitaxy. *Langmuir* 24: 5919–5924.

63. Takashiri, M., T. Shirakawa, K. Miyazaki, and H. Tsukamoto. 2007. Fabrication and characterization of bismuth–telluride-based alloy thin film thermoelectric generators by flash evaporation method. *Sens. Actuators A Phys.* 138: 329–334.

64. Takashiri, M., S. Tanaka, and K. Miyazaki. 2010. Improved thermoelectric performance of highly-oriented nanocrystalline bismuth antimony telluride thin films. *Thin Solid Films* 519: 619–624.

65. Das, V. D. and P. G. Ganesan. 1998. Thickness and temperature effects on thermoelectric power and electrical resistivity of $(Bi_{0.25}Sb_{0.75})_2Te_3$ thin films. *Mater. Chem. Phys.* 57: 57–66.

66. Duan, X. and Y. Jiang. 2010. Annealing effects on the structural and electrical transport properties of *n*-type $Bi_2Te_{2.7}Se_{0.3}$ thin films deposited by flash evaporation. *Appl. Surf. Sci.* 256: 7365–7370.

67. Venkatasubramanian, R., T. Colpitts, E. Watko, M. Lamvik, and N. El-Masry. 1997. MOCVD of Bi_2Te_3, Sb_2Te_3 and their superlattice structures for thin-film thermoelectric applications. *J. Cryst. Growth* 170: 817–821.

68. Venkatasubramanian, R., T. Colpitts, B. O'Quinn, S. Liu, N. El-Masry, and M. Lamvik. 1999. Low-temperature organometallic epitaxy and its application to superlattice structures in thermoelectrics. *Appl. Phys. Lett.* 75: 1104–1106.

69. Boulouz, A., S. Chakraborty, A. Giani, F. Pascal-Delannoy, A. Boyer, and J. Schumann. 2001. Transport properties of V–VI semiconducting thermoelectric BiSbTe alloy thin films and their application to micromodule Peltier devices. *J. Appl. Phys.* 89: 5009–5014.

70. Waters, J., D. Crouch, P. O'Brien, and J.-H. Park. 2003. Fabrication of thin films of bismuth selenide using novel single-source precursors by metal organic chemical vapor deposition. *J. Mater. Sci. Mater. Electron.* 14: 599–602.

71. Groshens, T. J., R. W. Gedridge, R. Scheri, and T. Cole. 1996. Low temperature MOCVD growth of V/VI materials via a Me_3SiNMe_2 elimination reaction. *15th International Conference on Thermoelectrics*, Pasadena, CA, March 26–29, 1996.

72. Giani, A., F. Pascal-Delannoy, A. Boyer, A. Foucaran, M. Gschwind, and P. Ancey. 1997. Elaboration of Bi_2Te_3 by metal organic chemical vapor deposition. *Thin Solid Films* 303: 1–3.

73. Giani, A., A. Boulouz, F. Pascal-Delannoy, A. Foucaran, E. Charles, and A. Boyer. 1999. Growth of Bi_2Te_3 and Sb_2Te_3 thin films by MOCVD. *Mater. Sci. Eng. B* 64: 19–24.

74. Giani, A., A. Boulouz, B. Aboulfarah et al. 1999. Effect of antimony concentration on the electrical and thermoelectrical properties of $(Bi_{1-x}Sb_x)_2Te_3$ thin films grown by metal organic chemical vapour deposition (MOCVD) technique. *J. Cryst. Growth* 204: 91–96.

75. Al Bayaz, A., A. Giani, A. Foucaran, F. Pascal-Delannoy, and A. Boyer. 2003. Electrical and thermoelectrical properties of Bi_2Se_3 grown by metal organic chemical vapour deposition technique. *Thin Solid Films* 441: 1–5.

76. You, H. W., S. H. Baek, K.-C. Kim, O. J. Kwon, J.-S. Kim, and Ch. Park. 2012. Growth and thermoelectric properties of Bi_2Te_3 films deposited by modified MOCVD. *J. Cryst. Growth* 346: 17–21.

77. Kang, S.-W., K.-M. Jeon, J.-S. Shin et al. 2013. MOCVD of c-oriented Bi_2Te_3 films on SiO_2 substrates using triethyl bismuth and di-tertiarybutyl tellurium. *Chem. Vapor Depos.* 19: 61–67.

78. Wang, G., L. Endicott, and C. Uher. 2011. Recent advances in the growth of Bi–Sb–Te–Se thin films. *Sci. Adv. Mater.* 3: 539–560.

79. Wang, G., L. Endicott, and C. Uher. 2015. Structure and transport properties of Bi_2Te_3 films. In *Thermoelectric Bi_2Te_3 Nanomaterials*, eds. O. Eibl, K. Nielsch, N. Peranio, and F. Völkline. pp. 73–98. Weinheim, Germany: Wiley-VCH Verlag GmbH & Co. KGaA.

80. Peranio, N., O. Eibl, and J. Nurnus. 2006. Structural and thermoelectric properties of epitaxially grown Bi_2Te_3 thin films and superlattices. *J. Appl. Phys.* 100: 114306.

81. Hansen, A.-L., T. Dankwort, M. Winkler et al. 2014. Synthesis and thermal instability of high-quality Bi_2Te_3/Sb_2Te_3 superlattice thin film thermoelectrics. *Chem. Mater.* 26: 6518–6522.

82. Liu, W., V. A. Stoica, H. Chi, L. Endicott, and C. Uher. 2015. Epitaxial growth and improved electronic properties of $(Bi_{1-x}Sb_x)_2Te_3$ thin films grown on sapphire (0001) substrates: The influence of Sb content and the annealing. *J. Alloys Compd.* 647: 50–56.

83. Liu, W., L. Endicott, V. A. Stoica, H. Chi, R. Clarke, and C. Uher. 2015. High-quality ultra-flat $BiSbTe_3$ films grown by MBE. *J. Cryst. Growth* 410: 23–29.

84. Cho, S., Y. Kim, A. DiVenere, G. K. Wong, J. B. Ketterson, and J. R. Meyer. 1999. Antisite defects of Bi_2Te_3 thin films. *Appl. Phys. Lett.* 75: 1401–1403.

85. Peranio, N., M. Winkler, D. Bessas et al. 2012. Room-temperature MBE deposition, thermoelectric properties, and advanced structural characterization of binary Bi_2Te_3 and Sb_2Te_3 thin films. *J. Alloys Compd.* 521: 163–173.

86. Aabdin, Z., N. Peranio, M. Winkler et al. 2012. Sb_2Te_3 and Bi_2Te_3 thin films grown by room-temperature MBE. *J. Electron. Mater.* 41: 1493–1497.

87. Peranio, N., M. Winkler, Z. Aabdin, J. König, H. Böttner, and O. Eibl. 2012. Room temperature MBE deposition of Bi_2Te_3 and Sb_2Te_3 thin films with low charge carrier densities. *Phys. Status Solidi A* 209: 289–293.

88. Winkler, M., X. Liu, J. D. Konig et al. 2012. Electrical and structural properties of Bi_2Te_3 and Sb_2Te_3 thin films grown by the nanoalloying method with different deposition patterns and compositions. *J. Mater. Chem.* 22: 11323–11334.

89. Haruhiko, O., H. Shun, O. Michihiro, Y. Atsushi, U. Kazuo, and I. Tsutomu. 2009. Thermoelectric properties of Bi_2Te_3-based thin films with fine grains fabricated by pulsed laser deposition. *Jpn. J. Appl. Phys.* 48: 085506.

90. Onose, Y., R. Yoshimi, A. Tsukazaki et al. 2011. Pulsed laser deposition and ionic liquid gate control of epitaxial Bi_2Se_3 thin films. *Appl. Phys. Express* 4: 083001.

91. Zhang, S. X., R. D. McDonald, A. Shekhter et al. 2012. Magneto-resistance up to 60 Tesla in topological insulator Bi_2Te_3 thin films. *Appl. Phys. Lett.* 101: 202403.

92. Gopal, R. K., S. Singh, R. Chandra, and Ch. Mitra. 2015. Weak-antilocalization and surface dominated transport in topological insulator Bi_2Se_2Te. *AIP Adv.* 5: 047111.

93. Symeou, E., M. Pervolaraki, C. N. Mihailescu et al. 2015. Thermoelectric properties of $Bi_{0.5}Sb_{1.5}Te_3$ thin films grown by pulsed laser deposition. *Appl. Surf. Sci.* 336: 138–142.

94. Chang, H.-C., C.-H. Chen, and Y.-K. Kuo. 2013. Great enhancements in the thermoelectric power factor of BiSbTe nanostructured films with well-ordered interfaces. *Nanoscale* 5: 7017–7025.

95. Walachová, J., R. Zeipl, J. Zelinka et al. 2005. High room-temperature figure of merit of thin layers prepared by laser ablation from Bi_2Te_3 target. *Appl. Phys. Lett.* 87: 081902.

96. Fan, P., Z.-H. Zheng, Z.-K. Cai et al. 2013. The high performance of a thin film thermoelectric generator with heat flow running parallel to film surface. *Appl. Phys. Lett.* 102: 033904.

97. Bourgault, D., C. G. Garampon, N. Caillault, L. Carbone, and J. A. Aymami. 2008. Thermoelectric properties of *n*-type $Bi_2Te_{2.7}Se_{0.3}$ and *p*-type $Bi_{0.5}Sb_{1.5}Te_3$ thin films deposited by direct current magnetron sputtering. *Thin Solid Films* 516: 8579–8583.

98. Liao, C.-N., X.-W. Su, K.-M. Liou, and H.-S. Chu. 2011. Electrical and thermal transport properties of electrically stressed Bi–Sb–Te nanocrystalline thin films. *Thin Solid Films* 519: 4394–4399.

99. Winkler, M., X. Liu, J. D. König et al. 2012. Sputtered *p*-type $Sb_2Te_3/(Bi,Sb)_2Te_3$ soft superlattices created by nanoalloying. *J. Electron. Mater.* 41: 1322–1331.

100. Winkler, M., X. Liu, A. L. Hansen et al. 2013. Sputtered *n*-type $Bi_2Te_3/(Bi, Sb)_2Te_3$ superlattice systems. *Nanothermoelectrics* 1: 1.

101. Liou, K. M. and C. N. Liao. 2010. Electric current enhanced defect elimination in thermally annealed Bi–Sb–Te and Bi–Se–Te thermoelectric thin films. *J. Appl. Phys.* 108: 053711.

102. Kim, D.-H., G.-H. Lee, and O.-J. Kim. 2007. The influence of post-deposition annealing on thermoelectric properties of Bi–Sb–Te films prepared by sputtering. *Semicond. Sci. Technol.* 22: 132.

103. Deng, Y., Z. Zhang, Y. Wang, and Y. Xu. 2012. Preferential growth of Bi_2Te_3 films with a nano-layer structure: Enhancement of thermoelectric properties induced by nanocrystal boundaries. *J. Nanopart. Res.* 14: 1–8.

104. Tan, M., Y. Deng, Y. Wang, B. Luo, L. Liang, and L. Cao. 2012. Fabrication of highly (00l)-textured Sb_2Te_3 film and corresponding thermoelectric device with enhanced performance. *J. Electron. Mater.* 41: 3031–3038.

105. Fan, P., T. Chen, Z. Zheng et al. 2013. The influence of Bi doping in the thermoelectric properties of co-sputtering deposited bismuth antimony telluride thin films. *Mater. Res. Bull.* 48: 333–336.

106. Taylor, A., C. Mortensen, R. Rostek, N. Nguyen, and D. C Johnson. 2010. Vapor annealing as a post-processing technique to control carrier concentrations of Bi_2Te_3 thin films. *J. Electron. Mater.* 39: 1981–1986.

107. Stoica, V. A., L. Endicott, H. H. Shen et al. 2014. High-quality II-VI films grown on amorphous substrates using tunable tetradymite templates. *Appl. Phys. Lett.* 105: 221606.

108. Winkler, M. 2015. Nanostructured thermoelectrics: Bi_2Te_3/Sb_2Te_3 based superlattice systems fabricated by MBE and sputtering. PhD dissertation, Eberhard Karls Universität Tübingen, Tübingen, Germany.

109. Chang, C.-Z., J. Zhang, X. Feng et al. 2013. Experimental observation of the quantum anomalous Hall effect in a magnetic topological insulator. *Science* 340: 167–170.

110. Hoefer, K., Ch. Becker, D. Rata, J. Swanson, P. Thalmeier, and L. H. Tjeng. 2014. Intrinsic conduction through topological surface states of insulating Bi_2Te_3 epitaxial thin films. *Proc. Natl. Acad. Sci. USA* 111: 14979–14984.

111. Kampmeier, J., S. Borisova, L. Plucinski, M. Luysberg, G. Mussler, and D. Grützmacher. 2015. Suppressing twin domains in molecular beam epitaxy grown Bi_2Te_3 topological insulator thin films. *Cryst. Growth Des.* 15: 390–394.

112. He, L., X. Kou, M. Lang et al. 2013. Evidence of the two surface states of $(Bi_{0.53}Sb_{0.47})_2Te_3$ films grown by van der Waals epitaxy. *Sci. Rep.* 3: 3406.

113. Zhang, J., C.-Z. Chang, Z. Zhang et al. 2011. Band structure engineering in $(Bi_{1-x}Sb_x)_2Te_3$ ternary topological insulators. *Nat. Commun.* 2: 574.

114. Xu, J.-P., M.-X. Wang, Z. L. Liu et al. 2015. Experimental detection of a Majorana mode in the core of a magnetic vortex inside a topological insulator-superconductor Bi_2Te_3/$NbSe_2$ heterostructure. *Phys. Rev. Lett.* 114: 017001.

115. Lee, J. J., F. T. Schmitt, R. G. Moore, I. M. Vishik, Y. Ma, and Z. X. Shen. 2012. Intrinsic ultrathin topological insulators grown via molecular beam epitaxy characterized by in-situ angle resolved photoemission spectroscopy. *Appl. Phys. Lett.* 101: 013118.

116. He, L., X. Kou, and K. L. Wang. 2013. Review of 3D topological insulator thin-film growth by molecular beam epitaxy and potential applications. *Phys. Status Solidi RRL* 7: 50–63.

117. Li, H. D., Z. Y. Wang, X. Kan et al. 2010. The van der Waals epitaxy of Bi_2Se_3 on the vicinal Si(111) surface: An approach for preparing high-quality thin films of a topological insulator. *New. J. Phys.* 12: 103038.

118. Zhang, G., H. Qin, J. Teng et al. 2009. Quintuple-layer epitaxy of thin films of topological insulator Bi_2Se_3. *Appl. Phys. Lett.* 95: 053114.

119. Bansal, N., Y. S. Kim, E. Edrey et al. 2011. Epitaxial growth of topological insulator Bi_2Se_3 film on Si(111) with atomically sharp interface. *Thin Solid Films* 520: 224–229.

120. Liu, C.-H. and J.-F. Jia. 2015. In situ electrical transport measurement of superconductive ultrathin films. *Chin. Phys. B* 24: 110702.

121. Cahill, D. G., W. K. Ford, K. E. Goodson et al. 2003. Nanoscale thermal transport. *J. Appl. Phys.* 93: 793–818.

122. Cahill, D. G., P. V. Braun, G. Chen et al. 2014. Nanoscale thermal transport. II. 2003–2012. *Appl. Phys. Rev.* 1: 011305.

123. Cahill, D. G. 1990. Thermal conductivity measurement from 30 to 750 K: The 3ω method. *Rev. Sci. Instrum.* 61: 802–808.

124. Cahill, D. G. 2002. Erratum: Thermal conductivity measurement from 30 to 750 K: The 3ω method [*Rev. Sci. Instrum.* 61: 802 (1990)]. *Rev. Sci. Instrum.* 73: 3701–3701.

125. Borca-Tasciuc, T., A. R. Kumar, and G. Chen. 2001. Data reduction in 3ω method for thin-film thermal conductivity determination. *Rev. Sci. Instrum.* 72: 2139–2147.

126. Dames, Ch. 2013. Measuring the thermal conductivity of thin films: 3 omega and related electrothermal methods. *Annu. Rev. Heat Trans.* 16: 7–49.

127. Völklein, F., H. Reith, A. Meier, and M. Schmitt. 2015. Measuring techniques for thermal conductivity and thermoelectric figure of merit of V–VI compound thin films and nanowires. In *Thermoelectric Bi_2Te_3 Nanomaterials*, eds. O. Eibl, K. Nielsch, N. Peranio, and F. Völkline. pp. 225–252. Weinheim, Germany: Wiley-VCH Verlag GmbH & Co. KGaA.

128. Hikami, S., A. I. Larkin, and Y. Nagaoka. 1980. Spin-orbit interaction and magnetoresistance in the two dimensional random system. *Prog. Theor. Phys.* 63: 707–710.

129. Brahlek, M., N. Koirala, M. Salehi, N. Bansal, and S. Oh. 2014. Emergence of decoupled surface transport channels in bulk insulating Bi_2Se_3 thin films. *Phys. Rev. Lett.* 113: 026801.

130. Wang, G., L. Endicott, H. Chi, P. Lošt'ák, and C. Uher. 2013. Tuning the temperature domain of phonon drag in thin films by the choice of substrate. *Phys. Rev. Lett.* 111: 046803.

131. Zhang, J., X. Feng, Y. Xu et al. 2015. Disentangling the magnetoelectric and thermoelectric transport in topological insulator thin films. *Phys. Rev. B* 91: 075431.

132. Xu, Y., Z. Gan, and S.-C. Zhang. 2014. Enhanced thermoelectric performance and anomalous Seebeck effects in topological insulators. *Phys. Rev. Lett.* 112: 226801.

133. Ghaemi, P., R. S. K. Mong, and J. E. Moore. 2010. In-plane transport and enhanced thermoelectric performance in thin films of the topological insulators Bi_2Te_3 and Bi_2Se_3. *Phys. Rev. Lett.* 105: 166603.

134. Shi, H., D. Parker, M.-H. Du, and D. J. Singh. 2015. Connecting thermoelectric performance and topological-insulator behavior: Bi_2Te_3 and Bi_2Te_2Se from first principles. *Phys. Rev. Appl.* 3: 014004.

135. Huang, B.-L. and M. Kaviany. 2008. *Ab initio* and molecular dynamics predictions for electron and phonon transport in bismuth telluride. *Phys. Rev. B* 77: 125209.

136. Xie, W., S. Wang, S. Zhu et al. 2013. High performance Bi_2Te_3 nanocomposites prepared by single-element-melt-spinning spark-plasma sintering. *J. Mater. Sci.* 48: 2745–2760.

137. Zhao, L. D., H. J. Wu, S. Q. Hao et al. 2013. All-scale hierarchical thermoelectrics: MgTe in PbTe facilitates valence band convergence and suppresses bipolar thermal transport for high performance. *Energy Environ. Sci.* 6: 3346–3355.

138. Chiritescu, C., C. Mortensen, D. G. Cahill, D. Johnson, and P. Zschack. 2009. Lower limit to the lattice thermal conductivity of nanostructured Bi_2Te_3-based materials. *J. Appl. Phys.* 106: 073503.

139. Takashiri, M., S. Tanaka, K. Miyazaki, and H. Tsukamoto. 2010. Cross-plane thermal conductivity of highly oriented nanocrystalline bismuth antimony telluride thin films. *J. Alloy. Compd.* 490: L44–L47.

140. Venkatasubramanian, R. 2000. Lattice thermal conductivity reduction and phonon localization-like behavior in superlattice structures. *Phys. Rev. B* 61: 3091–3097.

141. Winkler, M., X. Liu, U. Schürmann et al. 2012. Current status in fabrication, structural and transport property characterization, and theoretical understanding of Bi_2Te_3/Sb_2Te_3 superlattice systems. *Z. Anorg. Allg. Chem.* 638: 2441–2454.